Citation: He, Z., Guan, W., Wang, C., Guo, G., Zhang, L. & Gavaises, M. (2022). Assessment of turbulence and cavitation models in prediction of vortex induced cavitating flow in fuel injector nozzles. International Journal of Multiphase Flow, 157, 104251. doi: 10.1016/j.ijmultiphaseflow.2022.104251

This is the accepted version of the paper.

This version of the publication may differ from the final published version. To cite this item please consult the publisher's version.

Permanent repository link: https://openaccess.city.ac.uk/id/eprint/28804/

Link to published version: https://doi.org/10.1016/j.ijmultiphaseflow.2022.104251

Assessment of turbulence and cavitation models in prediction of vortex induced cavitating flow in fuel injector nozzles

Zhixia He[a,*,†]; Wei Guan[a,b,*]; Chuqiao Wang[b,c]; Genmiao Guo[a]; Liang Zhang[b]; Manolis Gavaises[c]

a. Institute for Energy Research, Jiangsu University, Zhenjiang 212013, China

b. School of Energy and Power Engineering, Jiangsu University, Zhenjiang 212013, China

c. School of Mathematics, Computer Science & Engineering, City, University of London, London, UK

Abstract

Vortex-induced cavitation develops in high pressure fuel injector equipment in areas where despite the very high surrounding pressures (>100 MPa), the rotational motion of the fluid causes large pressure drops in the core of a well-organized longitudinal vortex structure leading to cavitation with normally string type correspondingly also called string cavitation ; typically, the size of the string cavitation is small compared to the overall dimensions while they develop in a transient mode linked with the local flow turbulence. To address these complex interaction processes, some turbulence models have been tested in a diesel injector nozzle for which quantitative experimental data are available and are utilized to assess the predictive capability of relevant models; the flow has been considered compressible, turbulent and isothermal. The closure models considered include the RNG $k\!-\!\varepsilon$, SST $k\!-\!\omega$, RSM, WALE LES as well as a developed very-large eddy simulation model (VLES). The employed mass-transfer cavitation models are the Schnerr and Sauer (SS), Zwart-Gerber-Belamri (ZGB), HEM and a modified ZGB model with a self-adaptive adjustment of condensation coefficient. The results indicate that the RNG $k\!-\!\varepsilon$ model and SST $k\!-\!\omega$ model fail to predict the string cavitation induced by vortex flow in the

---

[*] The two authors contributed equally to this work.

[†] Corresponding author: Zhixia He E-mail address: zxhe@ujs.edu.cn

nozzle due to the drawback of the isotropic vortex-viscosity hypothesis. The RSM model could capture an acceptable string cavitation morphology. The numerical results utilizing the VLES model and LES model are in considerably good agreement with the experimental data, while the VLES model can provide the predictions of cavitating flow as precise as that using the LES model but on a much coarser mesh. The distributions of tangential velocity are similar to the velocity characteristics of Rankin vortex or Taylor vortex, which can help understand the coherent vortex structures in string cavitating flow. It is also shown that the RSM turbulence model with modified ZGB cavitation model improves the accuracy of prediction in the vortex-induced cavitation compared to the other three cavitation models.

Keywords: injector nozzle; string cavitation; turbulence model; cavitation model; vortex flow

1. Introduction

Atomizing liquid jets are realized in many application fields, such as internal combustion engines, rocket engines, medical sprays and material processing processes. Fuel atomization can improve engine combustion and emission performance vastly (Hu et al., 2020; Li et al., 2017; Wang et al., 2019; Zhang et al., 2020). Moreover, the injector nozzle internal flow, particularly in the presence of cavitation, has a pronounced effect on the fuel injection rate of the injection system as well as the subsequent spray characteristics, which triggers the actions to understand the nozzle cavitating flow thoroughly and optimize the injector design (Gavaises, 2008; Lan et al., 2020; Piscaglia et al., 2021; Som et al., 2011).

Cavitation forming inside nozzle holes is induced due to the huge pressure depressurization forcing large velocities that result to pressure drop below the fuel's vapour pressure. Such pressure locations are realized either at the entry to the hole orifices or at the core of the transient vortices developing within the sac volume and the injection holes (Battistoni et al., 2019; He et al., 2013; Koukouvinis et al., 2016; Sou et al., 2014; Trummler et al., 2021). Although the shed vortices generated from cavitation bubble collapses can increase the flow turbulence and promote the primary spray breakup, undesired effects such as the reduction of flow discharge coefficient and surface erosion need to be accounted for during injector design.

Vortex cavitation in particular was first observed within the SAC chamber of a diesel injector nozzle in (Arcoumanis et al., 1997; Kim et al., 1997). Some early experimental and computational studies have attempted to characterize the behavior of vortex cavitation in various nozzle types using high speed visualization and CFD. Gavaises et al. (Andriotis et al., 2008; Arcoumanis et al., 2000; Arcoumanis et al., 1999; Gavaises and Andriotis, 2006; Gavaises et al., 2009; Gavaises et al., 2008; Roth et al., 2002) revealed that the fluid flow passage in SAC chamber was related with needle lifts and SAC chamber shape largely, affecting the formation and development of string cavitation in an enlarged fully transparent nozzle. He et al. (Cao et al., 2020a; Zhang et al., 2018) pointed out that the increasing fuel temperature could accelerate the expansion of the string cavitation area in the large-scale tapered-hole nozzle. A fully developed string cavitation would increase pressure fluctuations (Cao et al., 2020b) in the hole and lead to a hollow-cone spray structure (Cao et al., 2020c) which is similar to the spray shape in the pressure-swirl atomizer (Laurila et al., 2020). Sou et al. (Prasetya et al., 2021; Pratama et al., 2017) experimentally verified that the stable string cavitation resulted in a widened fuel jet angle, and the formation mechanism of string cavitation was related with the fully developed vortex flow by the methods of visualization and PIV (particle image velocimetry) in a scaled-up nozzle. More recently, Karathanassis et al. (Karathanassis et al., 2017; Karathanassis et al., 2018) conducted X-ray Phase Contrast Imaging (XPCI), to capture the development of cavitating flow in nozzle holes in enlarged nozzle replicas. The X-ray tracer imaging method was also employed in the work of Moon et al. (Moon et al., 2019) that visualized the transient behavior of vortex-induced string cavitation in steel injector nozzles. However, the scale effect on string cavitation in enlarged injector nozzles is unclear (Arcoumanis et al., 2000; Guan et al., 2021a). The nuclei and micro-bubbles, cannot be scaled up in the liquid, but affect the growth and collapse of cavitation bubbles (Cao et al., 2021; Parkin, 1952). Accordingly, several studies have focused on the development of string cavitation in the real-size optical nozzle. The formation of string cavitation and its effects on spray plume, combustion and emission performance were studied in (Hayashi et al., 2013). Watanabe et al. (Watanabe et al., 2015) and He et al. (Chen et al., 2018; He et al., 2021) discussed the effects of various geometrical factors on the development of string cavitation and obtained abundant experimental data by visual investigations of the internal flow with real-size transparent injector nozzle tip under relatively high injection pressures. Still, limited information can be derived due to the very high velocities and short time scales.

Numerical simulations may provide more details of the vortex flow field and string cavitation inception and development process. However, the natural characteristics of an extensive range of spatial and temporal scales in transient string cavitating flow, related with vortex flow simultaneously, make numerical modeling computationally demanding. Different transient behaviors of vortex such as counter-rotating vortex and co-rotating vortex (Josserand and Rossi, 2007; Rojanaratanangkule and Tunkaew, 2016) may change the development of mainstream vortex and then further affect the transient characteristics of vortex-induced string cavitation. Therefore, selecting a turbulence model for reproducing such unsteady behaviors correctly is considerably significant (Chebli et al., 2021; Koukouvinis et al., 2017). The main numerical simulation methods for solving turbulence can be divided into three major categories roughly, i.e. Reynolds Averaged Navier-Stokes (RANS), Large Eddy Simulation (LES), and Direct Numerical Simulation (DNS). Both DNS and LES can reproduce the effects of turbulence structures and vortex dynamics in the flow accurately (Abdelsamie et al., 2021;

Gavaises et al., 2015; Trummler et al., 2020). In terms of DNS, very fine mesh resolution with a grid size set to the smallest flow scales (Kolmogorov scale) is needed, leading to prohibitive CPU times. In (Ohta and Sugiura, 2019), the interaction between wall turbulence vortices and vortex cavitation was also discussed with a proposed DNS method for compressible vapor-liquid turbulent flows. LES can resolve the large scale coherent turbulent scales with its acceptable grid burden accurately, which makes it prevailing in the current academic studies (Guo et al., 2017; Koukouvinis et al., 2016; Zhang et al., 2019). Some researchers (Kolovos et al., 2021; Naseri et al., 2018; Shi et al., 2016) investigated the coexistence of vortex-induced cavitation and geometry-induced cavitation using LES, but validations from experiment data were lacking. Piscaglia et al. (Piscaglia et al., 2021) compared the formation and development of string cavitation in two transparent injector nozzle replicas experimentally and those numerically with an LES-VOF multiphase solver. Nevertheless, RANS simulations still remain the mainstream approximation for simulating turbulent flow in engineering applications, attributing to lower computational cost and robustness (Xiao and Cinnella, 2019). In the prediction of cavitating flow, it is reported that RANS models might overestimate turbulent viscosity in cavitation zones. Therefore, a prevailing turbulent viscosity correction has been applied to reduce the eddy viscosity in mixture regions in the two-equation model (Reboud et al., 1998). Meanwhile, the defect of two-equation models is the isotropic hypothesis, which sometimes makes the models inapplicable in the swirling flow, despite some model modifications, such as a modification of the production term taking streamline curvature and system rotation effects into account (Shur et al., 2000; Spalart and Shur, 1997), may work in the simulation of vortex flow. Furthermore, Guan et al. (Guan et al., 2021b) obtained a slightly accurate string cavitation structure in an injector nozzle by the RSM model that abandons the isotropic eddy-viscosity hypothesis. The hybrid turbulence model is becoming more popular as it adopts the advantages of different modelling methods. VLES (Very-Large Eddy Simulation) model (Han and Krajnović, 2013a, b, 2015), one of the hybrid RANS-LES methods, attracted intensive interest. This model is a self-adaptive turbulence modeling method that can resolve the turbulence based on the local mesh resolution and the local turbulence scale information.

Cavitation also influences the local structure and dynamics of the vortex flow significantly (Cheng et al., 2020; Rinaldo et al., 2012). Cavitation models are based on different fundamental assumptions (Ghahramani et al., 2019; Kinzel et al., 2017; Koukouvinis et al., 2017; Kumar et al., 2020; Yamamoto et al., 2015). For vortex-induced string cavitation, strong turbulence vortices in the swirling flow lead to decreasing pressure in the vortex core dramatically, resulting in the generation of cavitation. In turn, the presence of cavitation may suppress turbulence fluctuation in the flow due to the intense rotation within the vortex core (Cotel and Breidenthal, 1999). Furthermore, compression and expansion of cavitation bubbles may affect the baroclinic torque in the vorticity transport equation and thus affect the turbulence vorticity (Dittakavi et al., 2010; Guan et al., 2021b; Koukouvinis et al., 2020; Li et al., 2019).

Various turbulence and cavitation model combinations can address different cavitating flow problems, especially for the special vortex-induced string cavitation in terms of complex interactions among vortex dynamics, turbulence structures and cavitation phase-change process investigated below. However, selecting diverse combinations of turbulence and cavitation model to describe the vortex-induced string cavitation more appropriately and the trade-off correlation between the precision and computational cost are not clear. Based on real-size optical nozzle internal transient flow experiment results from the high-pressure common-rail fuel injection system experiment set, the present paper presents put focus on a numerical study aiming to assess the predictive capability of turbulence and cavitation models to represent vortex-induced string cavitation. The turbulence models involved RNG

$k{-}\varepsilon$, SST $k{-}\omega$, RSM and WALE LES. A newly developed VLES model is introduced which enables a smooth, automatic conversion of turbulence simulation method between RANS and LES. The predictive capabilities of different turbulence models for string cavitation structures and flow characteristics are discussed, based on the validation against experimental data. In addition, reasons for prediction failures of traditional RNG $k{-}\varepsilon$ and SST $k{-}\omega$ models are analyzed. Meanwhile, the two-phase cavitation phase change and mass transfer is simulated by Schnerr and Sauer (SS) model (Sauer and Schnerr, 2000), Zwart et al. (ZGB) model (Zwart et al., 2004), a barotropic homogeneous equilibrium model (HEM). A modified ZGB cavitation model with a self-adaptive adjustment of condensation coefficient is proposed for improving the prediction accuracy of string cavitation structures and flow characteristics using RSM turbulence model. The injector geometric model utilised for the simulation in this work is the same one used in authors' former experimental published work (Chen et al., 2018; Guan et al., 2021b). The geometric parameters as well as experimental data in terms of spray cone angle, cavitation developing figures and et al. are utilised here for validation of the various numerical models investigated.

The paper is organized as follows: firstly, the numerical approaches utilised in this paper are introduced briefly; next, the visual experiment setup for the transient flow in a real-size optical injector nozzle and the detailed numerical approach are reported; afterwards, the effects of turbulence models on flow characteristics and string cavitation structure are discussed, and the comparisons of cavitation model performances used of simulation of string cavitation are shown. The most important conclusions are summarized at the end.

2. Description of the CFD approach

In the present work, the CFD code ANSYS Fluent was employed to simulate the two-phase with three components nozzle flow. As the scope of the present work is to simulate cavitation vortices, which have a distinct interface as opposed to cavitation clouds, the VOF method has been utilised instead of diffused interface approaches often employed for the simulation of cavitating flows in fuel injectors. The equations for continuity and momentum are as follows:

$$\frac{\partial \rho}{\partial t} + \nabla \cdot (\rho \boldsymbol{U}) = 0 \tag{1}$$

$$\frac{\partial \rho \boldsymbol{U}}{\partial t} + \nabla \cdot (\rho \boldsymbol{U}\boldsymbol{U}) = -\nabla P + \nabla \cdot \tau \tag{2}$$

where ρ is the density, $\boldsymbol{U}$ is the velocity, P is the pressure and τ is the mixture shear stress tensor. The properties in each cell are determined by its composition in each control volume. In each computational cell, the volume fraction of all phases sums to a value of unity. The following formulations are used to calculate mixture density and viscosity in each cell:

$$\rho = \sum_{m=1}^{n} \alpha_m \rho_m \tag{3}$$

$$\mu = \sum_{m=1}^{n} \alpha_m \mu_m \tag{4}$$

where α_m is the volume fraction of phase *m*. *n* equals to 3, hence the values of *m* are 1, 2 and 3, correspond to the subscripts *l*, *v* and *g*, which also denote liquid, vapor and gas (air). It is worth noting that n equals to 2 in the case of the barotropic HEM cavitation model. The values of m are 1 and 2, and correspond to the subscripts lv and g, which denote two-phase cavitating flow and gas (air). ρ and μ denote the density and the molecular viscosity, respectively. The mass conservation equations for the vapor and the air are as follows:

$$\frac{\partial \alpha_v \rho_v}{\partial t} + \nabla \cdot (\alpha_v \rho_v \boldsymbol{U}) = \dot{R}_e - \dot{R}_c \tag{5}$$

$$\frac{\partial \alpha_g \rho_g}{\partial t} + \nabla \cdot \left(\alpha_g \rho_g \boldsymbol{U}\right) = 0 \tag{6}$$

where the term $(\dot{R}_e - \dot{R}_c)$ are the phase change mass transfer rate between the liquid phase and vapor phase with respect to the growth and collapse process of vapor bubbles, while this terms is zero in the barotropic HEM cavitation modeling (Mithun et al., 2018). In a number of recent works from the authors, temperature and compressibility effects have been considered (Kolovos et al., 2021; Salemi et al., 2015; Strotos et al., 2015). However, such effects complicate the numerical solution; moreover, they have been applied within the diffuse interface framework. Considering that the focus of the paper is to resolve longitudinal vortex cavitation at normal fuel operating temperature within the injection orifice, where the variation of temperature does not vary more than 10 K for the pressure drops considered, the isothermal assumption has been adopted in the present study. Therefore, the energy conservation equation is not considered in the barotropic behavior of the fluid in this work. The applied diesel liquid properties (Kolev and Kolev, 2005; Payri et al., 2011) are functions of pressure only. The diesel vapor and air are assumed as incompressible gas. User-defined functions (UDFs) have been implemented for accounting diesel properties, modified ZGB cavitation, HEM cavitation model, VLES turbulence model and non-linear $k-\varepsilon$ model.

Prevailing modelling approach for cavitation flow are based on the simplified form of asymptotic Rayleigh-Plesset equation, including empirical calibrated terms for adjusting the mass transfer rate in different simulations. Two widely used models are Schnerr and Sauer (SS) model and Zwart et al. (ZGB) model. Moreover, homogenous equilibrium model (HEM) without any empirical parameters, linking pressure to density only, is examined in this study. HEM is more appropriate for modelling cavitating flows in diesel injector nozzle flows, but always needs higher grid resolutions and smaller time steps. A brief description is given about the formulation of these cavitation models applied in the present work in the Appendix 1; moreover, a modified ZGB model with a self-adaptive adjustment of condensation coefficient can be seen in the Appendix 1.4 which is based on the vortex intensity of the nozzle liquid flow.

Furthermore, the formation and collapse of cavitation are susceptible to two-way interaction between cavitation and turbulence. Compared with the cavitation model, the turbulence model is of vital importance for the description of string cavitation. The stretching term, related to the velocity gradient, is dominant in the formation and development of string cavitation (Guan et al., 2021b). Hence, the simulation accuracy can depend crucially on the turbulence model. Turbulence models can be classified as RANS models, like $k-\varepsilon, k-\omega$ and Reynolds stress equation model (RSM), Large Eddy Simulation (LES) model and hybrid models of RANS with LES. In this work, several well-known RANS models in terms of re-normalization group (RNG) $k-\varepsilon$, shear stress transport (SST) $k-\omega$ and linear strain pressure–strain (LRR) RSM, have been employed and compared. Meanwhile, the LES model including WALE (Wall- adapting local eddy viscosity model), and VLES model (Han and Krajnović, 2013a, 2015; Tiwari et al., 2020) are also investigated for applications in nozzle string cavitation flow simulations. A short introduction of applied turbulence models and details on derivation on VLES turbulence model are provided in Appendix 2.1 and Appendix 2.2.

3. Computational setup

3.1 Nozzle geometry and mesh topology

The previously introduced mathematical models have been used in the simulations of the flow characteristics in an injector nozzle. The simulated symmetric orifices injector nozzle replicates the geometrical topology of the real-size injector tip used in the experiments of the authors (Guan et al., 2021b). The tip of the actual metal nozzle is substituted by a transparent optical nozzle made of acrylic, as shown in Fig .1. The design parameters of the injector nozzle contain the hole inlet diameter D_{in} of 0.33 mm and hole exit diameter D_{out} of 0.26 mm, hole length L of 1.84 mm with a sharp-edge hole entrance, needle lift h of 0.3 mm and height of nozzle entrance H of 0.51 mm. The details of the experimental operation procedures and relevant experimental picture information were reported in (Chen et al., 2018; Guan et al., 2021b; He et al., 2016) and will not be repeated here.

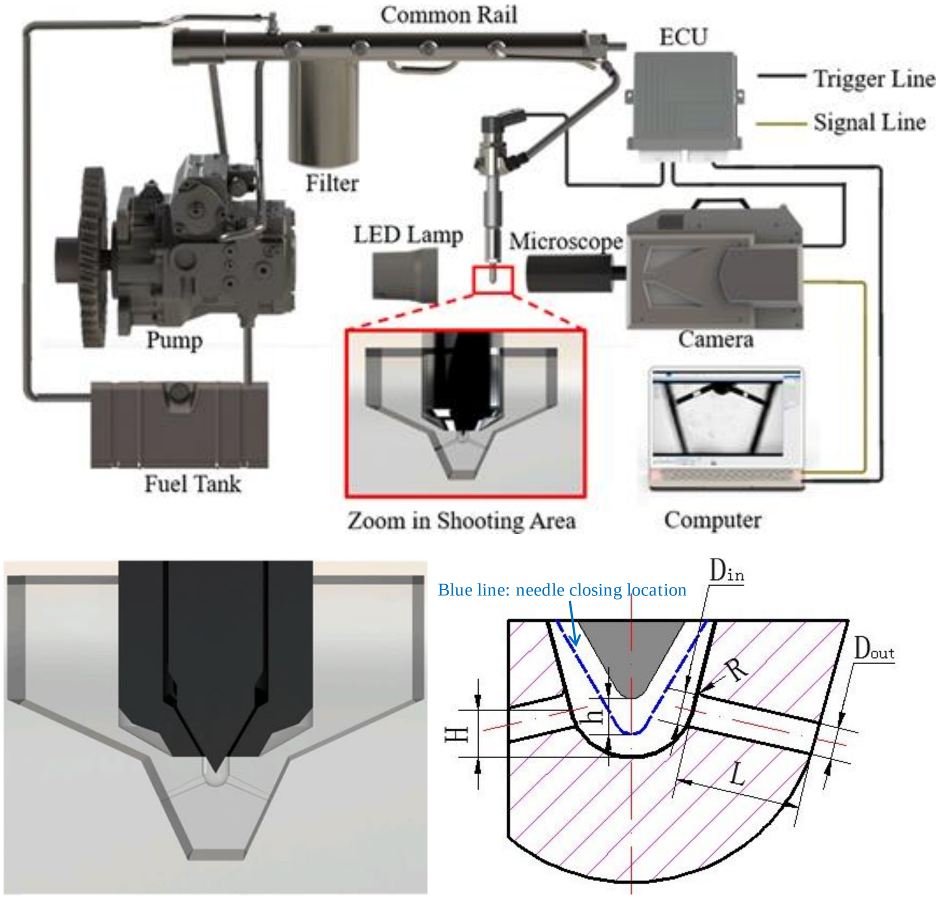

Fig. 1. The experimental set (top) and the real-size optical nozzle tip (bottom). The blue line represents the lowest needle location for the needle totally closing state. (Guan et al., 2021b; Wang et al., 2021)

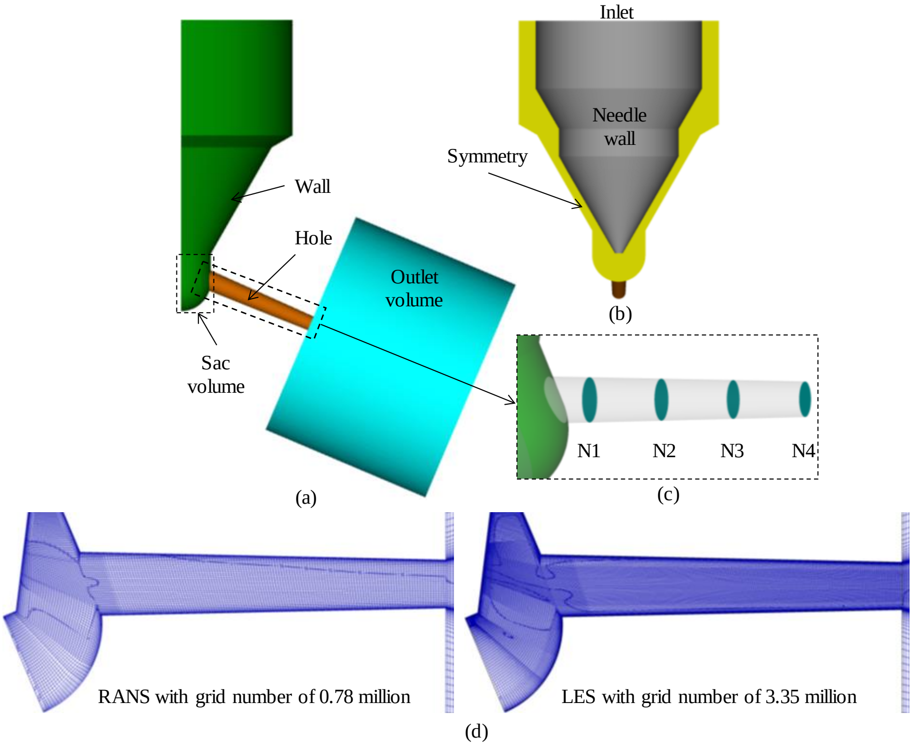

(a) (b) (c) (d)

Fig. 2. a)-b) Geometrical model and boundary conditions of injector nozzle; c) cross-planes along the nozzle; d) mesh resolutions of hole for RANS and LES models.

The nozzle hole is slightly tapered for the suppression of geometry-induced sheet cavitation, thus the clear presence of string cavitation in the injector nozzle hole becomes visible. The fixed injection pressure and backpressure are controlled steadily at 60 MPa and 0.1 MPa, respectively, which correspond to the working conditions in the transparent nozzle experiment. The geometry and mesh of the computational domain are illustrated in Fig. 2. The non-slip boundary condition is applied to the wall surfaces, and the symmetry boundary condition is adopted to reduce the computational burden. A back-pressure chamber is attached downstream the hole exit in order to move the outlet boundary condition away from the nozzle exit. Although the simulation is transient, the needle valve is assumed to be still at its maximum lift of 0.3 mm, where the experimental data indicate strong presence of vortex cavitation developing inside the hole orifices.

The computational mesh used for cavitating flow simulations is fully hexahedral. Grid refinement with sufficient resolution has been considered in the sac chamber and the central area of the hole orifice for resolving the sensitive area of string cavitation development. For RANS models, the mesh number of 0.78 million is appropriate to capture the characteristics of internal flow (Guan et al., 2021b), which will not be repeated here. As the truncation and subgrid stress modeling errors are reduced with increasing grid resolution, grid independence does not exist theoretically in large eddy simulations (LES). In order to adopt an appropriate mesh size, the Taylor micro-scales (λ_g) from the statistical theory of turbulence is often used as a common guideline for selecting the LES mesh in the relevant literature (Koukouvinis et al., 2017; Pope, 2001; Santos et al., 2020; Zhang et al., 2019).

$$\lambda_g = \sqrt{10} Re^{-0.5} L \approx 5.58\ \mu\mathrm{m} \tag{7}$$

As equation (7) suggests for the specific flow conditions simulated here, the maximum grid size in the hole is set to be similar to the Taylor length scale of 5 μm, as most flow features such as coherent vortexes can be captured with this grid size. The grid size near the hole wall is set to 0.5 μm with a cell growth ratio of 1.15 based on the turbulent boundary layer theory. y^+ is approximately 1 in the nozzle hole and less than 2 for the other part of the injector.

For the LES mesh quality evaluation, a special metric based on the turbulence resolution length scale is estimated (Celik et al., 2005; Santos et al., 2020).

$$\mathrm{LES\_IQ_v} = \frac{1}{1+0.05\left(\frac{\mu+\mu_t}{\mu}\right)^{0.53}} \tag{8}$$

where μ_t and μ are the sub-grid scale viscosity and laminar viscosity, respectively. The higher the value of this metric is, the better the resolution is (0.8 or above), similar to the ratio of resolved to total turbulent kinetic energy. In general, an acceptable LES will resolve at least 80% of the turbulent kinetic energy. The field of the LES quality metric LES_IQ_v is presented in Fig .3.

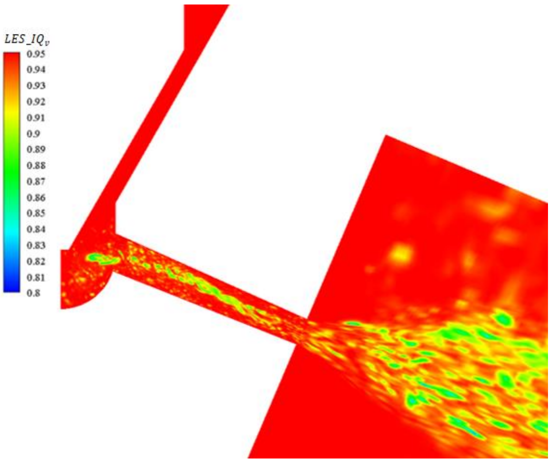

Fig. 3. LES quality metric for mesh quality evaluation.

The value of LES_IQ_v is mostly over 0.95 in the computational domain, while the minimum value is 0.85 roughly in the region where the string cavitation occurs. Consequently, the distribution of LES_IQ_v indicates that the LES mesh employed in this work is acceptable.

Moreover, for VLES an adjusting parameter has a value between 0 and 1.0 with the variation of mesh resolution, corresponding to the working turbulence models. Firstly, the same mesh resolution as that in RANS model is applied in the VLES simulation to judge whether the VLES model with the RANS grid resolution can capture the string cavitation. Afterwards, for obtaining the effect of different mesh resolutions in the VLES simulation, another mesh based on the LES mesh is generated, in which the maximum grid size is changed to 7.5 μm. The meshes employed for the different calculation cases are shown in Table 1.

Table 1. Mesh selection for different calculation cases.

Grid	Cells [in millions]	Maximum size in the hole [μm]	Turbulence models		
			RANS	LES	VLES
M0	0.78	10.0	√		√
M1	1.70	7.5			√
M2	3.35	5.0		√	

3.2 Fluid properties and solver setup

The density and viscosity of the fuel are calculated as a function of pressure in this work for considering the influence of fluid properties. The density and speed of sound values in liquid phase matches a interpolation formula from (Payri et al., 2011),

$$\rho = 835.698 - 0.628 \times 5 + 0.4914 \times (10^{-6}p - 0.1) - 0.00070499 \times (10^{-6}p - 0.1)^2 + 0.00073739 \times 5 \times 5 + 0.00103633 \times 5 \times (10^{-6}p - 0.1) \tag{9}$$

$$c = 1363.05 - 3.11349 \times 5 + 4.1751 \times (10^{-6}p - 0.1) - 0.00696763 \times (10^{-6}p - 0.1)^2 + 0.00940137 \times 5 \times (10^{-6}p - 0.1) \tag{10}$$

The liquid viscosity is based on the correlation proposed by (Kolev and Kolev, 2005).

$$\log_{10}\left(\frac{10^6 \mu_l}{\rho}\right) = 0.564676339 + 0.000388811 \times 10^{-5}p \tag{11}$$

Fig. 4 plots the density and viscosity values for different pressures at 303 K. The Tait equation of state fitted from the liquid density value for modeling the liquid phase of the barotropic HEM cavitation model. The other fluid properties involved are summarized in Table 2 and Table 3. Due to no air-suction in the nozzle, the incompressible air is set in this work.

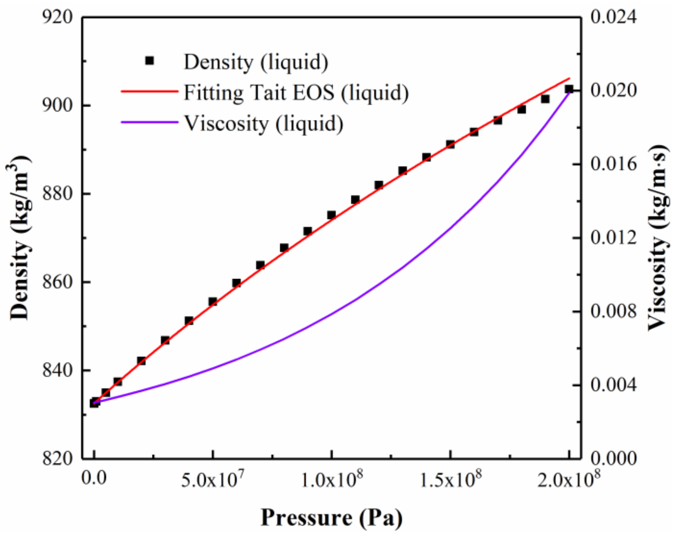

Fig. 4. Diesel fuel properties implemented with the variation of pressure.

Table 2. Thermodynamic properties for three phases with transport equation-based methods.

Liquid properties			Vapor properties			Air properties		
ρ_l	(Equation 9)	kg/m^3	ρ_v	0.1361	kg/m^3	ρ_{air}	1.165	kg/m^3
μ_l	(Equation 11)	kg/m-s	μ_v	7×10^{-6}	kg/m-s	μ_{air}	1.86×10^{-5}	kg/m-s

P_v	2000	Pa		

Table 3. Thermodynamic properties for three phases with the barotropic HEM model.

Liquid properties			Air properties		
B	$2.403e^8$	Pa	ρ_{air}	1.165	kg/m^3
$\rho_{sat,l}$	832.5278	kg/m^3	μ_{air}	1.86×10^{-5}	kg/m-s
μ_l	(Equation 11)	kg/m-s			
P_{sat}	2000	Pa			

The segregated and pressure-based solver is employed to solve the differential equations. Regarding the setting of the solution method, the pressure-velocity coupling scheme is taken with a SIMPLEC scheme. The cell gradients are calculated by using Least Square Cell Based method. The density is interpolated using a second order upwind scheme. Body force weighted scheme is selected for the pressure interpolation. The discretization of the vapor volume fraction transport equation is performed utilizing the Compressive scheme. The QUICK scheme is selected for the discretization of momentum equations for the RANS models, while the convective terms are discretized using a bounded central differencing scheme for the LES model and VLES models. Finally, time integration has been performed adopting a bounded second order implicit scheme. For the RANS models the time step is fixed as 3×10^{-8}s. For the others, an adaptive time step method is employed to ensure the Courant-Friedrichs-Lewy (CFL) number of 0.8 in the LES and VLES models, and of 0.5 in the barotropic HEM model. A proper flow initialization helps to obtain the accurate flow field quickly. The simulations have been carried out initially under the steady-state cavitation condition. Then, the unsteady cavitating flow is simulated for the first 200 μs to reduce the effect of the initial value. Finally, the simulation is sequentially carried out for a duration of addition 200 μs. This time interval corresponds to ~40 times of the residence time of the flow inside the hole orifice, assuming an average velocity in the direction of the hole of

~350m/s for the given pressure drop of 60MPa and a discharge coefficient of ~0.7.

4. Results and Discussion

The comparison of numerical and experimental results is reported below. It is worth noting that the time-averaged experimental values have been obtained by the in-house imaging processing code performed in MATLAB. Since the vortex cavitation development is more obvious at the maximum needle lift, this condition was chosen to compare the numerical results and experimental data. The time interval of 890μs (maximum lift holding time) with a total of 90 consecutive experimental pictures from the experiment was selected for average processing, while the numerical calculation time is excerpted as 200μs out of 890μs for time averaging.

4.1 Effect of turbulence models

Validations of numerical models by comparison with experimental data are shown in Fig. 5 and Fig. 6. The time-averaged simulation results of vapor iso-surfaces, tangential velocity vectors and pressure contours for the RANS cases are shown in Fig. 5, and the simulation results with the same data processing as above mentioned applied for LES and VLES models are shown in Fig.6. The solid red line shown in the velocity and pressure distribution plots at nozzle hole cross sections denotes the region of vortex-induced string cavitation occurring. The cavitation phase-change mass transfer model applied in these simulations is the ZGB cavitation model.

In Fig. 5, it can be seen that the SST $k\!-\!\omega$ turbulence model hardly reproduces vortex-induced string cavitation in the injector nozzle, and only a small amount of vapor phase occurs at the hole exit. Moreover, no significant low-pressure regions with large pressure gradients are witnessed at the nozzle hole cross section planes. Weak swirling flow hardly captures the low-pressure region in the vortex core, resulting in no phase transition. The prediction of the RNG $k\!-\!\varepsilon$ model is slightly better than that of the SST $k\!-\!\omega$

model. Thin string cavitation structures are detected at both the inlet and outlet of the hole with the RNG $k-\varepsilon$ model. The RSM model is superior to both above-mentioned models in the prediction of string cavitation. Besides, at the both inlet and outlet region of the hole, the intense string cavitation is also captured in the nozzle sac volume. The comparison between the RSM simulation result and the experimental data shows a close match in the string cavitation morphology. However, the fracture of string cavitation in the simulation occurs in the central orifice area frequently; therefore it is unable to capture the continuity of cavitation morphology present in the experiment. The published paper reported that the transient string cavitation in the central orifice area appeared intermittently as the RSM model was using (Guan et al., 2021b). When applying the RNG $k-\varepsilon$ model and RSM model, the low-pressure regions are evident on the center of nozzle section planes while the pressures at the vortex core fail to reach saturated vapor pressure. Although there are same model corrections for swirling flow, both models have difficulty to reproduce the same string cavitation as the experimental shadowgraph. However, by adjusting the empirical parameters of the RSM model predictions closer to the experimental data can be obtained.

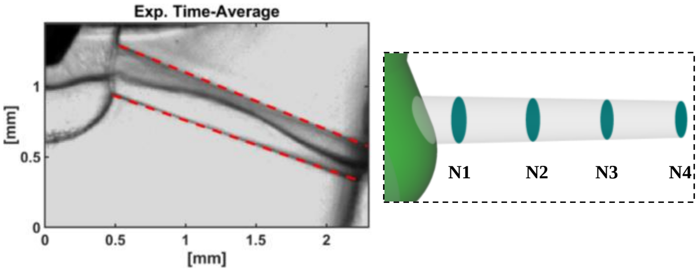

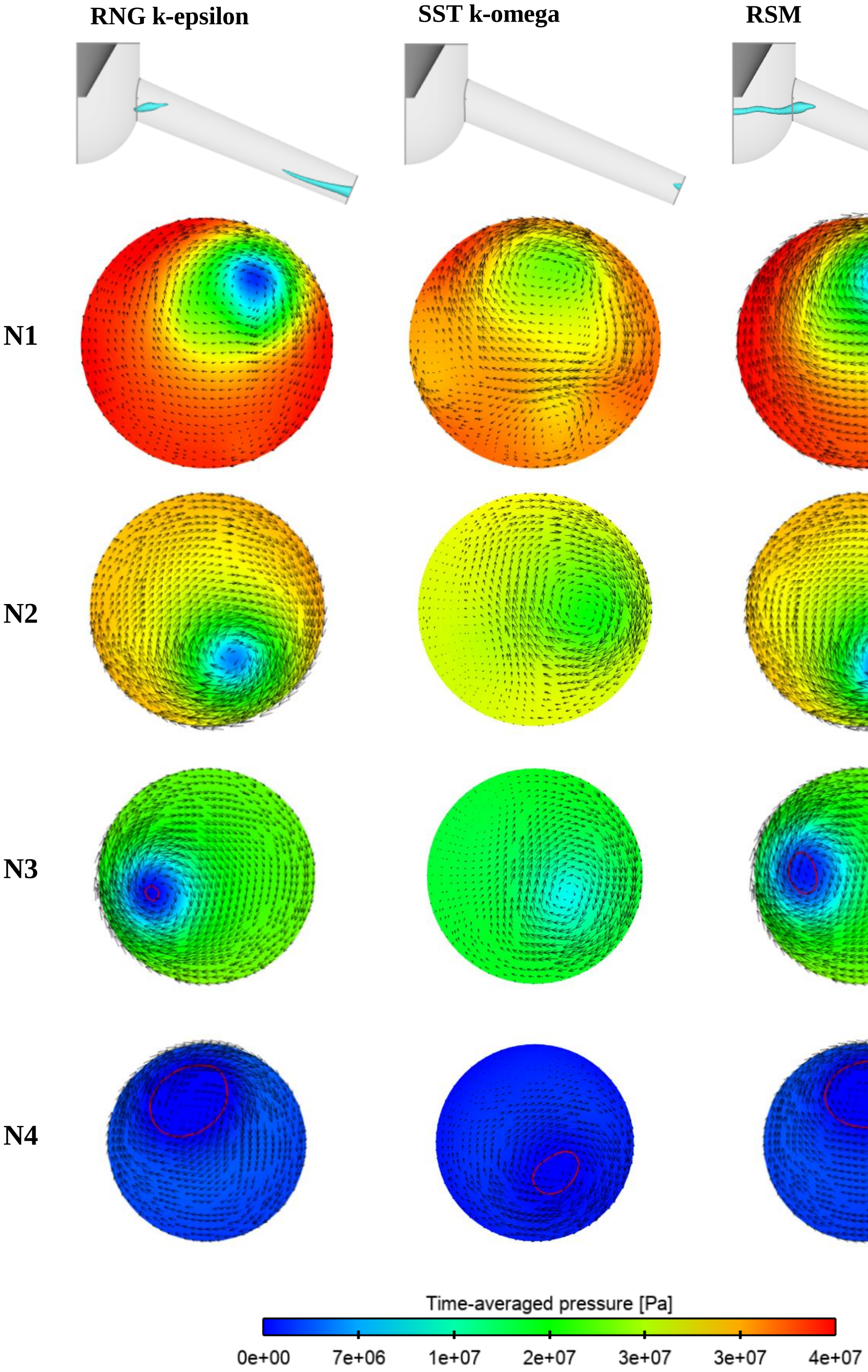

Fig. 5. Comparisons of experimental string cavitation distribution and numerical results (αv = 0.1) adopting RANS turbulence models (Grid M0). Time-averaged tangential velocity vectors and pressure contours on the four planes (N1, N2, N3 and N4) which are indicated in Fig .2. The red line shows the region of detected cavitation structures.

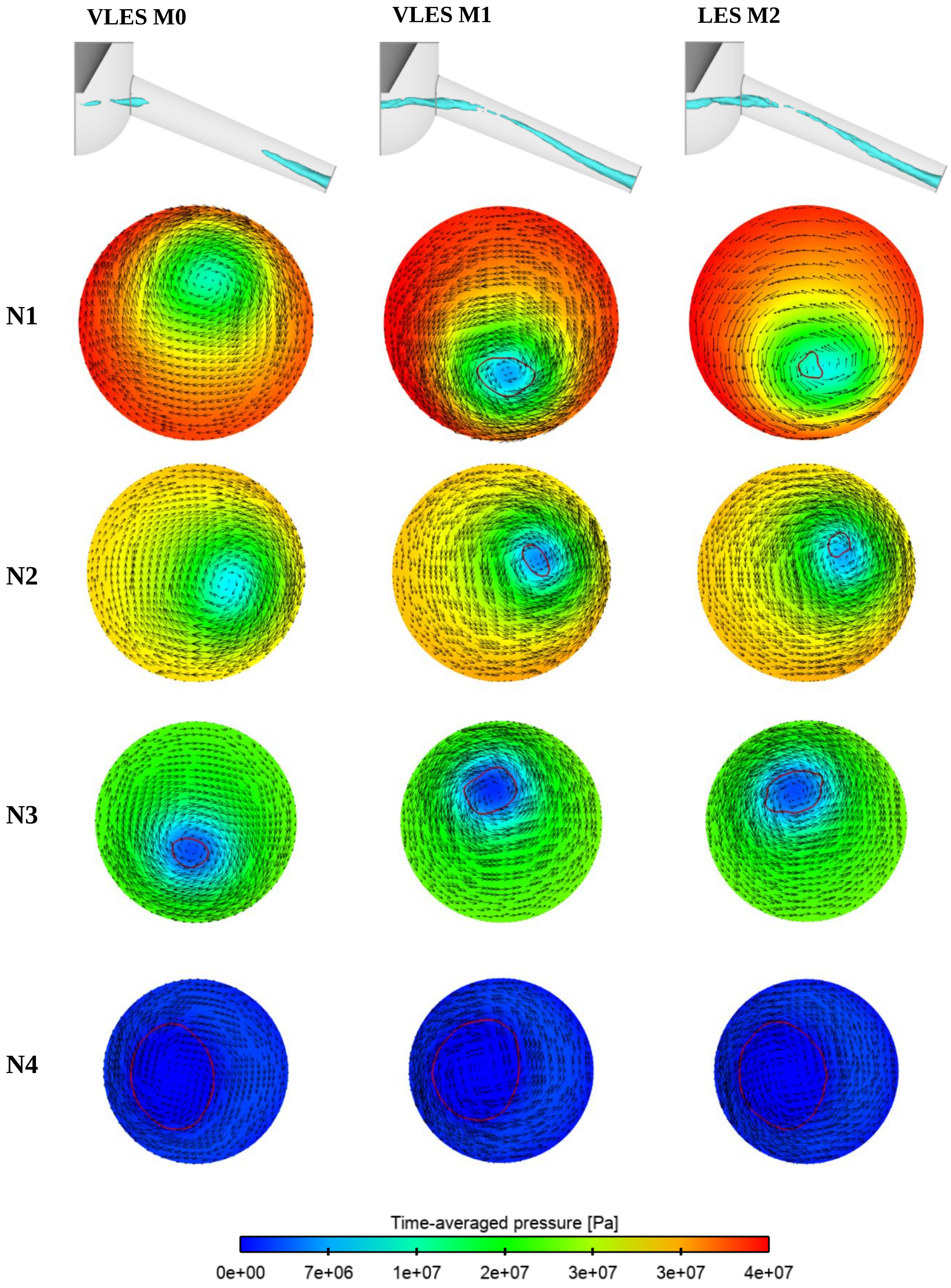

Fig. 6. Comparison of experimental string cavitation distribution and numerical results (αv = 0.1) adopting LES (Grid M2) and VLES models (Grid M0 and M1). Time-averaged tangential velocity vectors and pressure contours on the four planes (N1, N2, N3 and N4) which are indicated in Fig .2. The red line shows the region of detected cavitation structures.

In Fig. 6, the time-averaged string cavitation morphologies using the VLES M and LES M2 models are highly consistent with the experimental data, i.e., the string cavitation is generated throughout the sac chamber and nozzle length. The string cavitation and the corresponding low-pressure regions are detected on the section planes across the hole length. Notably, due to the transient instability characteristics of cavitating flow in the VLES and LES calculations, the time average processing reduces the pressure gradient under large pressure difference (pressure-inlet: 60 MPa and saturated vapor pressure: 0.002 MPa) so that the time-averaged low-pressure area is not conspicuous. The VLES result using the M1 grid is similar to that adopting the LES model obtained with the M2 grid, but requires about half of its computational time. The accuracy of the LES model is highly dependent on grid requirements. Pope (Pope, 2004) points out that LES simulation can be considered effective as the analytical kinetic energy reaches 80% of total kinetic energy; this was used as the rule-of-thump for selecting the M2 grid. However, a satisfactory result can still be obtained in the VLES simulation of coarser gird M1, which is unable to meet the computational grid requirements for LES. In addition, the VLES result using even much less grid M0 is slightly inferior to those in other cases, but the string cavitation intensity is still stronger than those utilizing the RNG $k-\varepsilon$ model and SST $k-\omega$ model, as shown in Fig. 5. Therefore, the calculation results of the VLES model are slightly less sensitive to the grid requirements. It is worth noting that the accuracy of VLES calculations is able to approach the calculation accuracy in RANS models, as the grid size reaches a specific range where the adjustment coefficient Fr is close to 1.

Fig. 7 shows the evaluations of vapor area coefficient along the normalized hole length using different turbulence models. The vapor area coefficient, which can be considered as spatial string cavitation intensity, is defined as the ratio of vapor area at the hole slice ($\alpha_v > 0.1$) to the hole slice area. The experimental data is obtained by imaging processing performed in MATLAB, in which the area coefficient is calculated by the ratio of a grey area (normalized grey value > 0.5) to the hole slice area. It should be noted here that only the length coefficient of vapor phase at the hole slices can be calculated by obtaining the pixel width in terms of pixels due to the available two-dimensional experimental images; accordingly, a hypothesis that the string cavitation structure approximates a cylinder is applied to eventually acquire the vapor area coefficient. The other illustration should be noted is about the selection of the grey threshold. Due to the experimental limitation, such as image noise and pixel density, as well as the fuzzy cavitation interface, the value of the grey threshold is set to a value of 0.5 in this study.

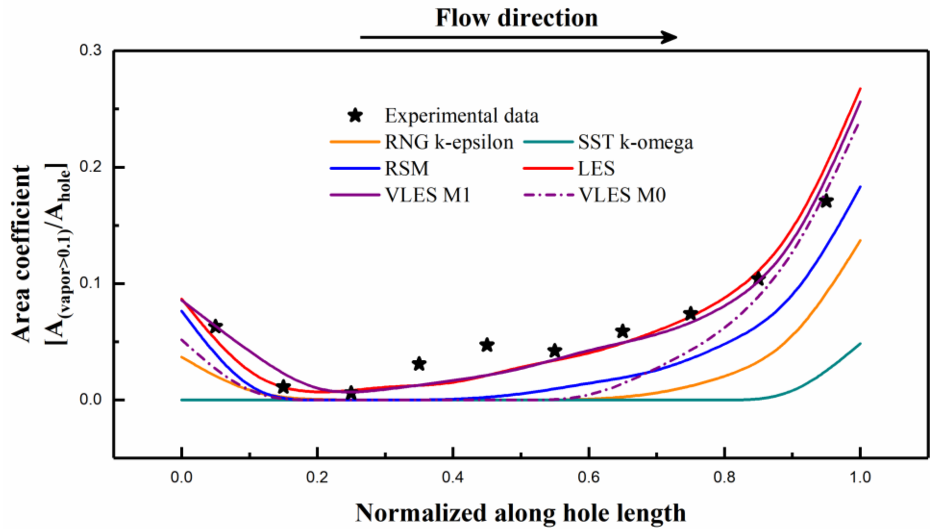

Fig. 7. Numerical time-averaged vapor area coefficient using different turbulence models and experimental time-averaged area coefficient along the hole length.

As shown, the VLES (M1) and LES models give more accurate predictions for the vapor area coefficient, which shows a good agreement with the string cavitation intensity as derived from the experimental data. The vapor area coefficient drops down towards the middle of the nozzle hole, then rises beyond the 30% of the hole lenght and reaches the highest value down to the hole exit. It demonstrates that the regions prone to occurrence of string cavitation are concentrated near the entrance and exit of the injector nozzle hole, especially in the vicinity of the hole outlet. However, the other three turbulence models in the RANS family fail to predict the vapor area coefficient in the entire hole length accurately. These discrepancies can also confirm the RANS models especially the RNG $k\text{−}\varepsilon$ model and SST $k\text{−}\omega$ model, are not able to capture the string cavitation.

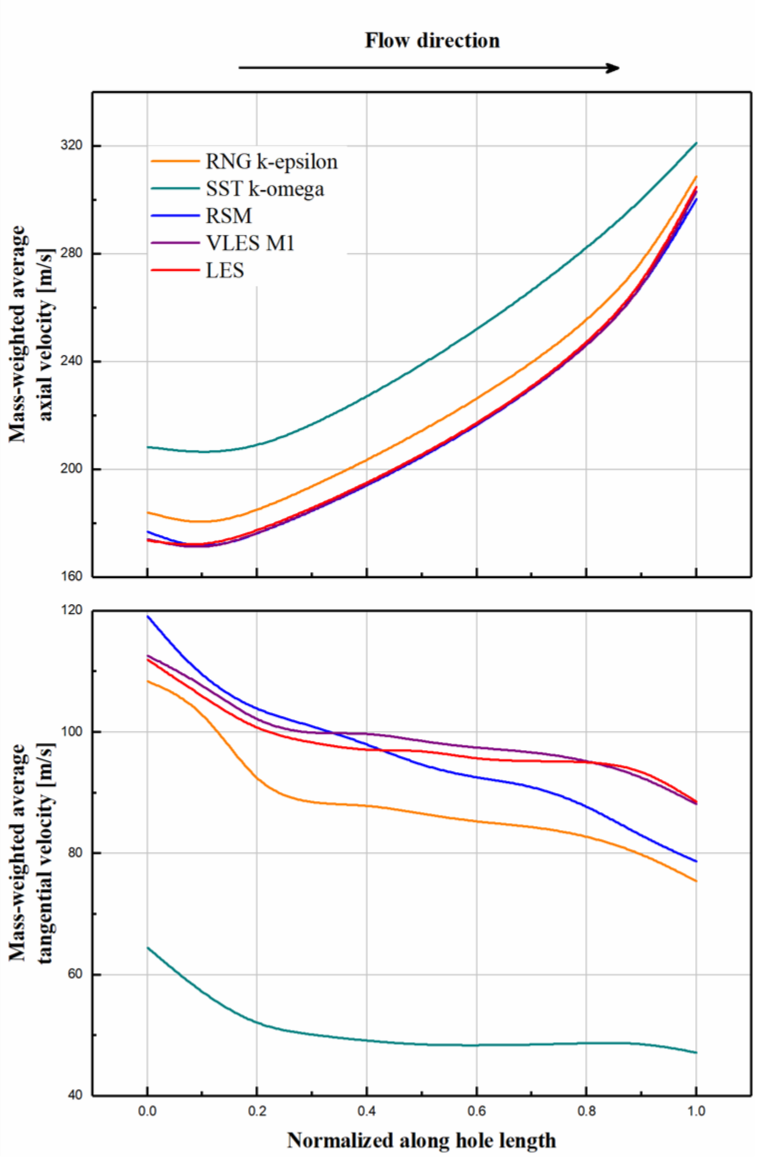

Fig. 8. Time-averaged mass-weighted average tangential velocity and axial velocity along the hole length using different turbulence models.

In Fig. 8, the time-averaged mass-weighted tangential and axial velocities along the entire hole length are displayed. Axial components of flow velocity are increasing significantly along the injector nozzle hole due to the effect of nozzle conicity regardless of turbulence models. For the cases utilizing the RNG $k-\varepsilon$ and SST $k-\omega$ models, weaker swirling flows which correspond to lower tangential velocities in the nozzle hole consequentially give rise to higher axial velocities. While for the RSM model, VLES M1 and LES models, the curves of axial velocity almost overlapped. A closer examination in Fig. 8 reveals that the tangential velocity using SST $k{-}\omega$ model along the hole length is only half compared to the predictions obtained with the rest of the turbulence models. Moreover, the progressively increasing axial velocity along the nozzle hole also leads to the decrease of the tangential velocity, which contradicts the progressively increasing of string cavitation intensity, as shown in Fig. 7. A noticeable consensus tells that higher tangential velocity stands for stronger string cavitation. This opposite conclusion can be explained from the following aspect:

According to the modeling of the Rankine vortex, the decrease of surrounding fluid pressure will trigger the decrease of pressure in the vortex core, as shown in the following equation.

$$\text{Rankine vortex:} \quad \begin{cases} p = p_\infty - \frac{\rho\Gamma^2}{4\pi^2 r_0^2}\left(1 - \frac{r^2}{2r_0^2}\right), & r \le r_0 \\ p = p_\infty - \frac{\rho\Gamma^2}{8\pi^2}\frac{1}{r^2}, & r \ge r_0 \end{cases} \tag{12}$$

where Γ is vortex circulation. p_∞ and p are surrounding fluid pressure and vortex core pressure, respectively. r_0 is vortex core size. As illustrated in Fig.5 and Fig. 6, the pressure is gradually reduced along the nozzle hole due to the tapered nozzle hole. It implies that the pressure outside the vortex core will be lower, which results to expansion of the volume of the string cavitation. As a result, the slight reduction of tangential velocity barely makes a difference on the string cavitation structure downstream along the nozzle hole.

The variations of time-averaged flow discharge coefficient at the hole outlet and vapor volume in the nozzle hole for the injector are illustrated in Fig. 9. The time-averaged discharge coefficient Cd_{avg} is defined according to the following equations:

$$Cd_{avg} = \frac{\bar{m}}{m_{th}} = \frac{\bar{m}}{A_{out}\sqrt{2\rho_l \Delta P}} \tag{13}$$

$$Cd_{avg} = \frac{\bar{m}}{m_{th}} = \frac{\overline{A_{eff}}}{A_{out}} \cdot \frac{\overline{U_{eff}}}{U_{th}} \frac{\rho_l}{\rho_l} = C_a \cdot C_v \tag{14}$$

where $\bar{m}$ and m_{th} are the average mass flow rate from the simulation and the theoretical mass flow rate calculated according to the Bernoulli equation, respectively. A_{out} and ΔP refer to the hole outlet area and the pressure difference between the pressure at inlet and outlet. In Equation 14, U_{th} is the theoretical velocity calculated by the Bernoulli equation. $\overline{A_{eff}}$ and $\overline{U_{eff}}$ are the average effective area and velocity at the hole outlet respectively. C_a and C_v are the area coefficient and velocity coefficient at the hole outlet.

The flow discharge coefficients calculated from the simulation applying the RNG $k-\varepsilon$ and SST $k-\omega$ models are both larger compared to those using the other turbulence models. This is because the string cavitation intensities simulated using both RNG $k-\varepsilon$ model and SST $k-\omega$ model models are weaker, and correspondingly the volumes of vapor phase in the hole are smaller. As depicted in Fig. 7 and Fig. 8, the axial velocities and liquid area coefficients (1.0 minus vapor area coefficient) adopting the RNG $k-\varepsilon$ model and SST $k-\omega$ model are relatively higher, corresponding to a higher area coefficient C_a and velocity coefficient C_v as shown in Equation 14. The flow discharge coefficients of the RSM model, VLES model and LES model are fairly close, except that the flow discharge coefficients got from simulations using RSM model are slightly higher. This is due to the same axial velocities in Fig. 8 and a higher liquid area coefficient simulated utilizing the RSM model in Fig. 7. Moreover, although the flow discharge coefficients calculated from the VLES M0, VLES M1 and LES models are almost the same, there are still some differences in the volume of vapor phase in the hole among them.

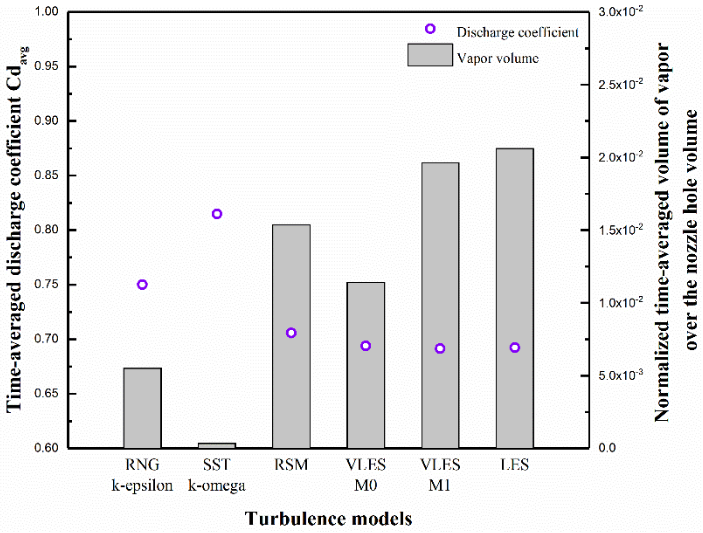

Fig. 9. Time-averaged flow discharge coefficient and vapor volume from simulations applying different turbulence models.

In Fig. 10 (a), the plot of time-averaged vapor fraction and tangential velocity along the target line radius direction of hole exit section is given. The schematic diagram of the target line is shown in Fig. 10 (b), with the red dashed line connecting the hole exit section center (C1, purple solid point) and vortex core center (C2, blue solid point). It can clearly be seen that the distribution of vapor fraction along the target line is shaped like a "hill" with the value being high in the middle and low on both ends. Large amounts of diesel vapor are generated at the center of the hole exit section due to the local low-pressure region in the large vortex core, as illustrated in Fig. 5 and Fig. 6. Moreover, the cavitation region is characterized by eccentricity, i.e., misalignment of the hole exit center and vortex core center. It can be inferred that the subsequent spray cone angle will present a considerably asymmetry characteristic. For the VLES M1 and LES models, the cavitation vapor distributions are approximately overlapping. The areas of cavitation vapor simulated using the VLES M and LES models are larger compared to those predicted by RNG $k{-}\varepsilon$, SST $k{-}\omega$ and RSM models; in particular, the area of cavitation vapor simulated utilizing SST $k{-}\omega$ model is the lowest.

Furthermore, Fig. 10 (a) reveals that the tangential velocity at the vortex core where the highest diesel vapor fraction occurs is relatively low, then increases to both sides along the target line progressively as depicted in Fig. 10 (b), finally approaches the value of zero at the hole wall. It is worth mentioning that the tangential velocities obtained from simulations utilizing the RNG $k-\varepsilon$ model and RSM model are not equal to zero due to the effect of the applied wall function in the simulations. The distribution of tangential velocity can be approximated to the characteristics of either Rankin vortex or Taylor vortex, as illustrated in Fig. 10 (c). Due to the viscous effect, the tangential velocity distribution inside and outside the vortex core should follow a smooth transition. Therefore, the Taylor vortex should be closer to physical reality, and its analytical solution can help further understanding the coherent vortex structure in string cavitating flow. Meanwhile, the concise analytical solution of the Rankin vortex can also help to develop more suitable physical models such as those of (Zhao et al., 2016). Likewise, for the cases applying the VLES M1 and LES models, the tangential velocity distributions are approximately overlapping, which can further highlight the advantages of the VLES model for capturing the string cavitation in the injector nozzle.

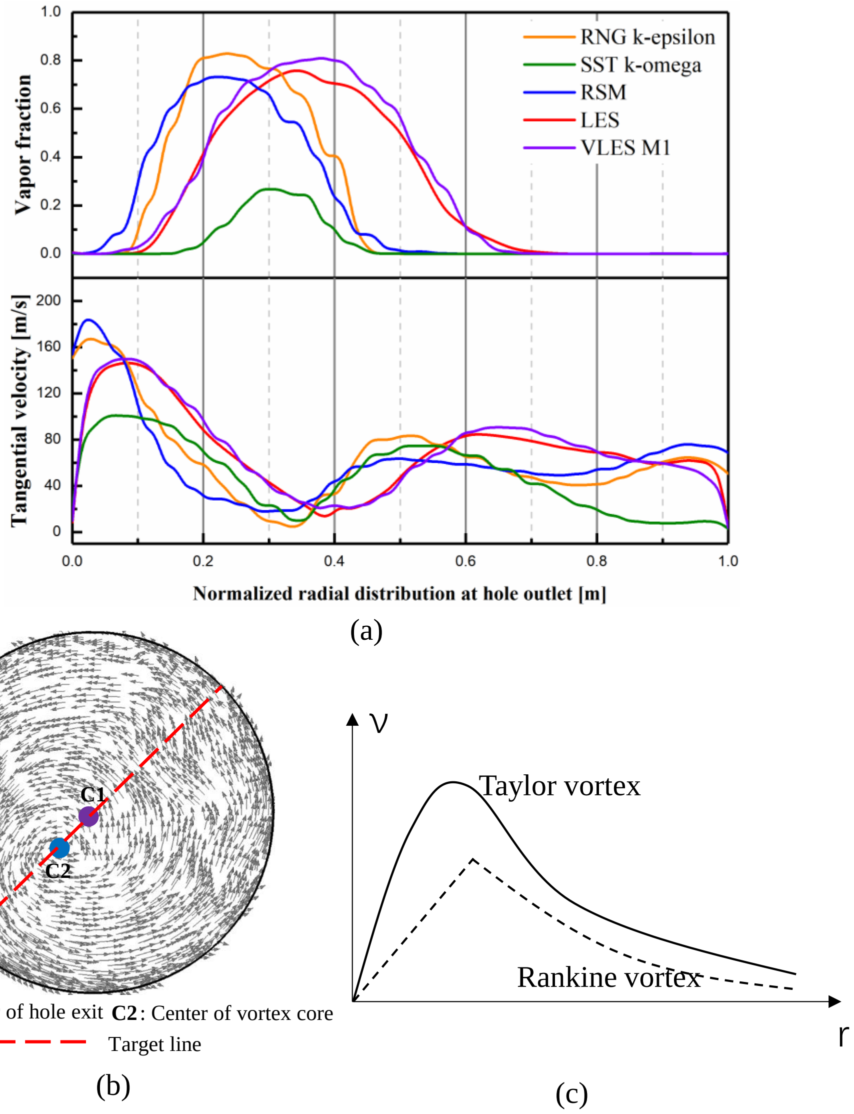

(a)

(b)

(c)

Fig. 10. (a) Time-averaged vapor fraction and tangential velocity versus radial distribution at hole exit. (b) Schematic diagram of target line at hole exit. (c) Schematic view of the distributions of tangential velocity along vortex core radius in Taylor vortex and Rankine vortex.

The comparisons of Reynolds shear stress and mean strain rate on nozzle hole slices (N1, N2, N3 and N4) got from simulations applying LES model are shown in Fig. 11. Considering of the overlap of the central axis of nozzle hole and the X axis, the Reynolds shear stress component and the corresponding mean strain rate are defined as:

$$\overline{v'w'} = \overline{(v_i - \bar{v})(w_i - \bar{w})} \tag{15}$$

$$\epsilon_{yz} = \epsilon_{zy} = \frac{1}{2}\left(\frac{\partial v}{\partial z} + \frac{\partial w}{\partial y}\right) \tag{16}$$

It is worth noting that the above Reynolds stress equation only contains the term related to velocity. A closer examination in Fig. 11 demonstrates that the Reynolds shear stress is not aligned with the corresponding mean strain in the nozzle cross-section planes, which is similar to the findings of (Chow et al., 1997; Jiang et al., 2008). Generally, for the isotropic vorticity model for turbulent closure in RANS, the shear stress is aligned with the mean strain rate:

$$\overline{\mathrm{u_i}'\mathrm{u_j}'} \propto \left(\frac{\partial \mathrm{U_i}}{\partial \mathrm{x_j}} + \frac{\partial \mathrm{U_j}}{\partial \mathrm{x_i}}\right) \tag{17}$$

Therefore, the linear relationship between Reynolds shear stress and mean strain rate in the simulation of vortex-induced string cavitation is hardly valid in the injector nozzle, which explains the poor predictions applying RNG $k{-}\varepsilon$ model and SST $k{-}\omega$ model in this simulation. On the contrary, the RSM model can mostly predict the dynamic characteristics of string cavitation, on account of abandoning the isotropic vortex-viscosity hypothesis and considering the rate of rotation term for the mean velocity field. Moreover, Liu et al. (Liu et al., 2016; Wang and Liu, 2018) developed a nonlinear $k{-}\varepsilon$ model, which also abandons the isotropic vortex-viscosity hypothesis and verifies the predictive ability of this model on the tip vortex cavitation flow. In this section, a nonlinear $k{-}\varepsilon$ model is also applied to calculate the string cavitation in the injector nozzle. The equations can be found in (Ehrhard, 1999; Heschl et al., 2005). Fig. 12 shows the comparison of the time-averaged iso-surface of string cavitation utilizing the RSM and the nonlinear $k{-}\varepsilon$ models. The string cavitation structure simulated utilizing the nonlinear $k{-}\varepsilon$ model is similar to that using the RSM model, but both are unable to obtain sufficiently accurate prediction results compared to experimental data.

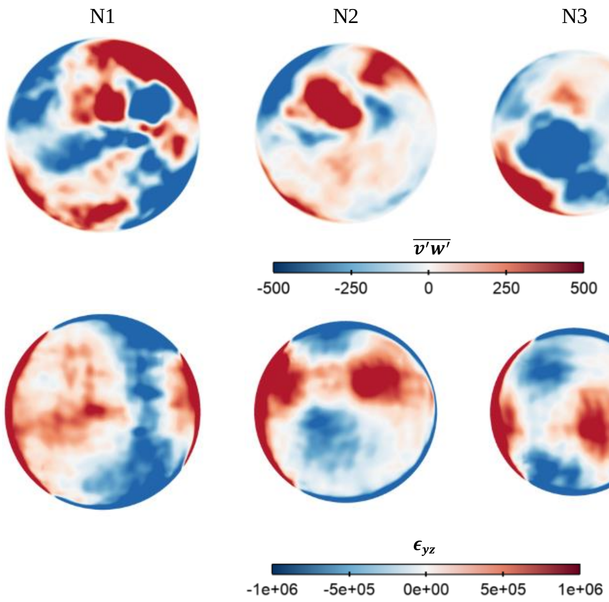

Fig. 11. Time-averaged contours of Reynolds shear stress component (top) and mean strain rate (bottom) on four cross-section planes of the nozzle hole with LES model.

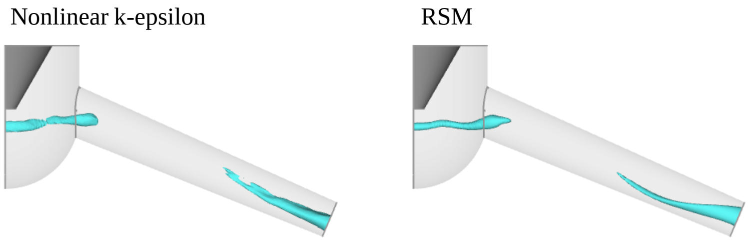

Fig. 12. Time-averaged iso-surface of string cavitation applying RSM model and nonlinear $k\!-\!\varepsilon$ model.

4.2 Cavitation model analysis

Besides different turbulence models, different cavitation models have been also considered. Fig. 13 shows the time-averaged string cavitation structures simulated with different cavitation models. The solid lines with four colors present the outlines of cavitation region in four different nozzle hole slices (N1, N2, N3 and N4). Although the prediction ability of the RSM turbulence model is weaker than those of the VLES and LES models, its computing mesh and physical time are much smaller, with a better predictive capability of string cavitating flow when compared to the other RANS turbulence models.

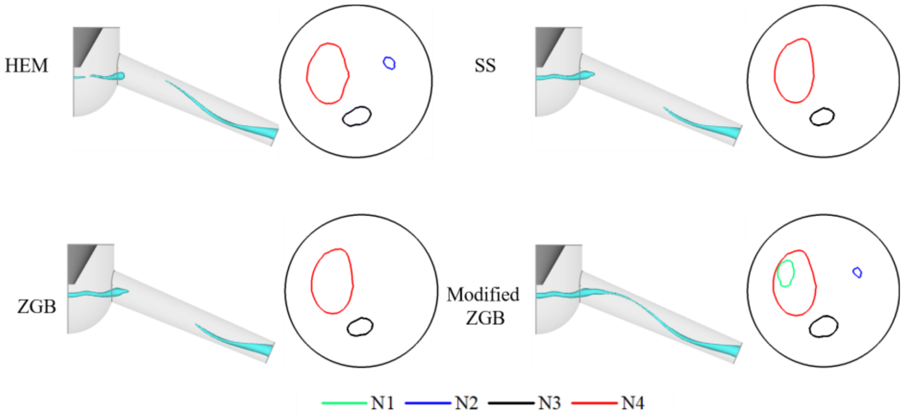

Fig. 13. Comparison of time-averaged cavitation structures ($\alpha_v = 0.1$) adopting different cavitation models from time-averaged experimental shadowgraph (top). The different colors of solid line symbolize the outlines of string cavitation in four cross-section planes.

From Fig. 13, the numerical results using the SS model and ZGB model are similar, showing the intense string cavitation captured in the SAC chamber as well as both the inlet and outlet of the nozzle hole. Only in the plane N3 and N4, string cavitation structures are captured. For the HEM model, less string cavitation volume is generated in the SAC chamber. While in the nozzle hole, the length of the string cavitation is longer comparing the SS and ZGB model, indicating a more similar shape with experimental data. Furthermore, HEM model with infinite mass transfer rate demonstrates a better prediction ability because string cavitation structures are captured in the planes N2, N3 and N4, one more plane than those using SS and ZGB model with certain finite mass transfer rate. This advantage may be attributed to the compressible form of diesel liquid phase and vapor phase. According to the analysis of the vorticity transport equation (Guan et al., 2021b), the compressibility of both phases in this simulation may increase the importance of the vorticity dilation term, which reflects the effects of fluid compressibility on the vorticity variation. However, all above mentioned three models failed to capture the continuous morphology of the string cavitation flow within the nozzle hole, especially the middle part of the nozzle. This drawback could be overcome by applying the new modified ZGB cavitation model mentioned in Appendix 1.4, it could be clearly seen that the string cavitation structure presents the continuous feature and consistent with that in the experimental data approximately. In addition, string cavitation structures are well captured in not only the plane N2, N3 and N4, but also the plane N1. The results indicate that the string cavitation generated in the SAC chamber could develop further downstream, keeping its original trajectory with the modification of the condensation coefficient.

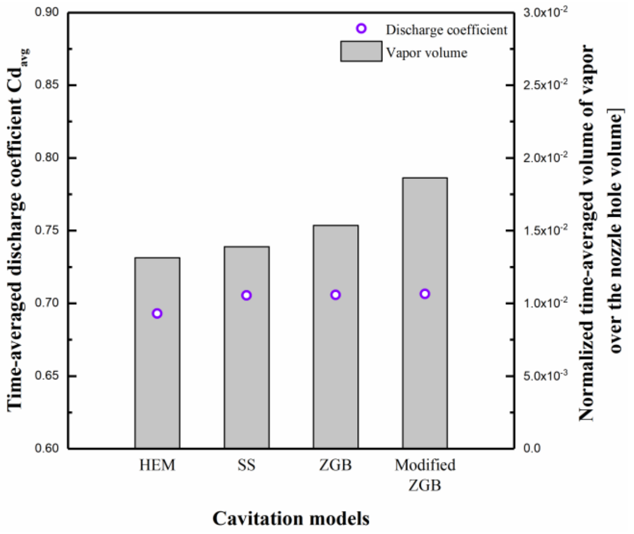

Fig. 14. Time-averaged flow discharge coefficient and vapor volume applying different cavitation models.

Fig. 14 demonstrates the variations of time-averaged flow discharge coefficient at the hole outlet and vapor volume in the nozzle hole for the injector. The discrepancies of flow discharge coefficient from simulations using four cavitation models are relatively small, despite the discharge coefficient from simulations using the HEM cavitation model is lower. Meanwhile, different cavitation models do not affect the flow characteristic in the injector nozzle. In terms of vapor volume in the hole, the cavitation volume generated adopting the modified ZGB cavitation model is the highest because the self-adaptive adjustment of the condensation coefficient delays the breakup of cavitation bubbles. The vapor volume simulated using the ZGB cavitation model is also larger than that utilizing the SS cavitation model; therefore, the ZGB cavitation model is applied to calculate the cavitation phase change mass transfer in the previous section. For the HEM cavitation model, due to the unsatisfactory prediction of string cavitation in the SAC chamber, the cavitation volume in the nozzle hole is lowest. Moreover, although the HEM cavitation model can obtain a relatively acceptable string cavitation structure in the nozzle hole as shown in Fig. 13, poor robustness and long calculation time for the HEM model in pressure-based solver make the simulation difficult to converge, determining the modified ZGB cavitation model for modeling mass transfer in the previous section is adopted.

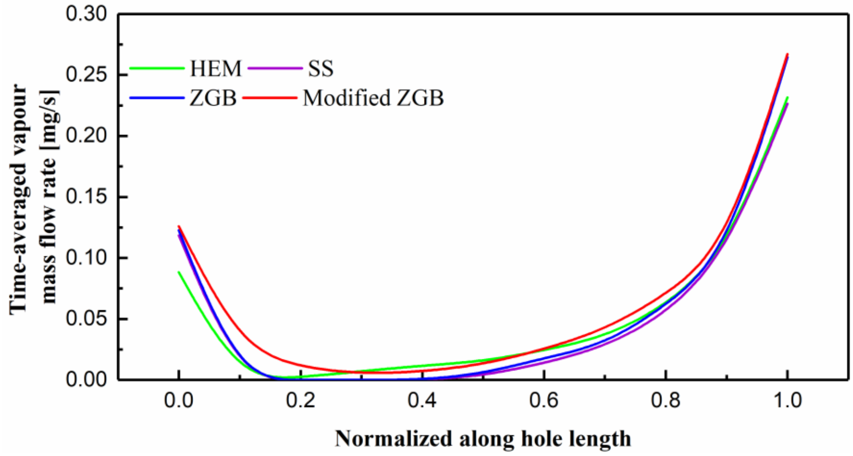

Fig. 15. Time-averaged vapor mass flow rate along the hole length applying different cavitation models.

The different cavitation models affect the amount of vapor mass in the nozzle hole, as shown in Fig. 15. Resulting from the relative weaker string cavitation generated in the SAC chamber, the vapor mass flow rate at the entrance of the nozzle hole is the lowest. The values of vapor mass flow rate using the ZGB cavitation model and SS cavitation model are overlapped. For the modified ZGB cavitation model, due to the self-adaptive adjustment of the condensation coefficient, the vapor mass flow rate at the hole entrance is the highest. In addition, in the middle of the hole, the vapor mass flow rates utilizing the modified ZGB cavitation model and HEM cavitation model are higher than those adopting the ZGB cavitation model and SS cavitation model, attributing to the considering of the fluid compressibility for the HEM model and the reduction of condensation coefficient for modified ZGB model. At the hole exit, the overlapped values of vapor mass flow rate applying the modified ZGB cavitation model and ZGB cavitation model are higher than those using the HEM cavitation model and SS cavitation model.

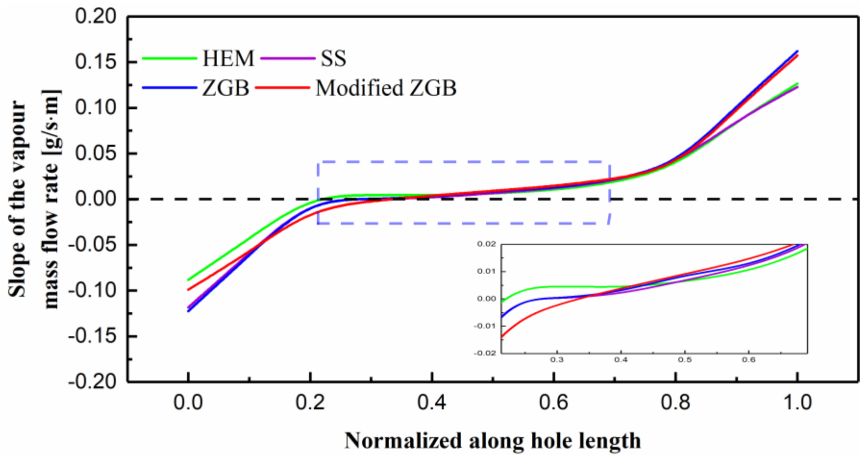

Fig. 16. Slope of the vapor mass flow rate along the hole length applying different cavitation models.

Fig. 16 demonstrates the slope of the vapor mass flow rate along the hole length. The positive values and negative values present the net evaporation and condensation per meter of the hole length, respectively. Combined with Fig. 15, at the hole entrance, the values of condensation for HEM cavitation model and modified ZGB cavitation model are higher than those for ZGB cavitation model and SS cavitation model. The formal is due to weak string cavitation generated in SAC chamber, while the latter is because of the self-adaptive adjustment of condensation coefficient. A closer examination reveals that the flow at the hole entrance is complex and chaotic that a steady coherent vortex is unable to survive (Guan et al., 2021b); resulting in prevailing the condensation process. At the hole middle and exit, a vigorous coherent vortex supports the generation of string cavitation, and the evaporation process is predominant, as illustrated in Fig. 16. It is also found that the values of evaporation in the modified ZGB cavitation model and ZGB cavitation model gradually exceed those in the HEM cavitation model and SS cavitation model.

5. Conclusions

This paper numerically evaluates the predictive capability of turbulence models and cavitation models applications in simulations of the vortex-induced string-type cavitation flow in a diesel injector tapered-hole nozzle. The turbulence models investigated here includes RNG $k-\varepsilon$ model, SST $k-\omega$ model, RSM model, LES model and a newly developed VLES model. The cavitation liquid-vapor phase change mass transfer is governed by cavitation models in terms of SS model, ZGB model, barotropic HEM model and a new modified ZGB model. Numerical results are presented as the diesel vapor iso-surfaces to be compared with experimental data. Main conclusions are summarized as follows:

(1) RNG $k-\varepsilon$ model and SST $k-\omega$ model fail to reproduce vortex-induced string cavitation in the injector nozzle due to their isotropic eddy viscosity hypothesis. For the nozzle transient string cavitating flow, the Reynolds shear stress is not aligned with the corresponding mean strain, therefore, RSM model can capture a more accurate string cavitation structure slightly.

(2) The cavitation morphologies simulated using the LES model and VLES model are highly consistent with experimental data. Although the grid resolution of VLES model is far below than the LES model, a satisfactory result could still be obtained. Thus, the VLES model can keep the balance between computational accuracy and efficiency.

(3) The flow discharge coefficients calculated from simulations applying the RSM model, VLES model and LES model are fairly close and smaller than those using the RNG $k-\varepsilon$ model and SST $k-\omega$ model. The performances of velocity and pressure in string cavitating flow are approximated to the characteristics of Rankin vortex or Taylor vortex, which can help understanding the vortex-induced string cavitation and develop appropriate models.

(4) The string cavitation structure simulated adopting the modified ZGB cavitation model is approximately consistent with experimental data. Although the HEM model can reproduce a slightly more accurate string cavitation structure in the hole, it fails to calculate the complete string cavitation in the SAC chamber. The predictive capability of the ZGB model and SS model on string cavitation is close, and ZGB cavitation is more suitable.

Different model combinations can address diverse cavitating flow problems in engineering applications and academic researches. This research suggests that, the RSM turbulence model combined with the modified ZGB cavitation model could be used to perform the multi-parameter analysis such as the effect of geometrical factors and dynamic factors on the development of string cavitation with less computational resources. The VLES model combined with the ZGB cavitation model could be employed to capture more details on vortex characteristics of super high-speed, transient and intense turbulent flow in the injector nozzle with an acceptable computational cost, particularly for a strong coherent vortex. The LES model with the ZGB cavitation model may be applicable to investigate the interaction between cavitation bubbles, fuel jet and surrounding air in the primary spray.

Acknowledgements

The authors would like to appreciate the help in VLES (Very-large eddy simulation) model supported by Xingsi Han from Nanjing University of Aeronautics & Astronautics.

This research was supported by the National Key Research and Development Project of China (2019YFB1504004), National Natural Science Foundation of China (No. 51776088, 52106155, 52106153), Natural Science Foundation of Jiangsu Province of China (SBK2021044559), China Postdoctoral Science Foundation (No. 2020TQ0126) and Research Innovation Plan for Postgraduates in Jiangsu Universities of China (KYCX20_3023).

Appendix 1. Cavitation models

1.1 Schnerr and Sauer cavitation model (S-S)

The Schnerr and Sauer cavitation model (Sauer and Schnerr, 2000) assumes the vapor phase consists of numerous mini spherical bubbles, and the liquid and vapor phases are in thermodynamic equilibrium. The condensation and vaporization rates are defined as:

$$\dot{R}_e = \frac{\rho_l \rho_v}{\rho}\alpha_v \alpha_l \frac{3}{R_B}\sqrt{\frac{2}{3}\frac{(P_v - P)}{\rho_l}} \quad P_v \geq P \tag{18}$$

$$\dot{R}_c = \frac{\rho_l \rho_v}{\rho}\alpha_v \alpha_l \frac{3}{R_B}\sqrt{\frac{2}{3}\frac{(P - P_v)}{\rho_l}} \quad P_v \leq P \tag{19}$$

where $\dot{R}_e$ and $\dot{R}_c$ are the rates of condensation and vaporization, respectively. Schnerr and Sauer use the following expression to connect the vapor volume fraction to the number of bubbles per unit volume of pure liquid n and generic bubble radius R_B:

$$\alpha_v = \frac{n\frac{4}{3}\pi {R_B}^3}{1 + n\frac{4}{3}\pi {R_B}^3} \tag{20}$$

here, the value of n as 10^{13} is chosen in this work.

1.2 Zwart-Gerber-Belamri cavitation model (ZGB)

The ZGB model (Zwart et al., 2004) assumes that all the bubbles in a system have the same size. In the ZGB model, the Rayleigh relation for the description of bubbles growth and collapse is also used. The final expressions of the cavitation model are as follows:

$$\dot{R}_e = F_{\mathrm{vap}} \frac{3\alpha_{\mathrm{nuc}}(1-\alpha_{\mathrm{v}})\rho_{\mathrm{v}}}{R_{\mathrm{B}}}\sqrt{\frac{2}{3}\frac{(p_{\mathrm{v}} - p)}{\rho_{\mathrm{l}}}} \quad p \leq p_{\mathrm{v}} \tag{21}$$

$$\dot{R}_c = F_{\mathrm{cond}} \frac{3\alpha_{\mathrm{v}}\rho_{\mathrm{v}}}{R_{\mathrm{B}}}\sqrt{\frac{2}{3}\frac{(p - p_{\mathrm{v}})}{\rho_{\mathrm{l}}}} \quad p > p_{\mathrm{v}} \tag{22}$$

where F_{vap} and F_{cond} are empirical coefficients, and equal to 50 and 0.01, respectively (Zwart et al., 2004). Both empirical coefficients also need to be calibrated according to some specific cavitation problems. Significantly, by increasing the transfer rates to infinity, the model will tend to a barotropic cavitation model asymptotically (Koukouvinis et al., 2017). R_{B} represents the mean radius of bubbles, which is assumed to be 0.001 mm in this model.

1.3 Barotropic HEM cavitation model

For the barotropic HEM cavitation model, the phase change between the liquid and vapor is considered via the EoS. In this model, the mass transfer occurs instantaneously, and the density variations are linked to the pressure evolution strongly (Gold et al., 2019; Koukouvinis et al., 2017). Thus, no empirical parameters and tuning are needed.

A two-step barotropic equation of state is employed in this work (Egerer et al., 2014; Kyriazis et al., 2017; Papoutsakis et al., 2020). The Tait EoS is used for the liquid phase. The isentropic-resembling process is employed for the liquid-vapor mixture.

$$p(\rho) = \begin{cases} (B + p_{sat})\left[\left(\frac{\rho}{\rho_{sat,l}}\right)^n\right] - B & \rho \geq \rho_{sat,L} \\ p_{sat} + C\left[\frac{1}{\rho_{sat,l}} - \frac{1}{\rho}\right] & \rho < \rho_{sat,L} \end{cases} \tag{23}$$

The speed of sound is calculated by the square root of first derivative of the equation (24) and given as follows:

$$c(\rho) = \begin{cases} Bn\frac{\rho^{n-1}}{\rho_{sat,l}^{n}} & \rho \geq \rho_{sat,L} \\ \frac{C}{\rho^2} & \rho < \rho_{sat,L} \end{cases} \tag{24}$$

The volume fraction of the vapor phase in a computational cell is computed from the density of the liquid vapor mixture as follows:

$$\alpha_v = \frac{\rho_{sat,l} - \rho_{lv}}{\rho_{sat,l} - \rho_v}, \text{ if } \rho_{lv} < \rho_{sat,l} \tag{25}$$

where factor B stands for the bulk modulus of liquid. Exponent n represents the stiffness of the Tait EoS which is usually set as 7.15 for the weakly compressible liquid (Ivings et al., 1998; Koukouvinis et al., 2017). In the isentropic process for the mixture, C is 1347.069 Pa kg/m3. p_{sat} is the saturation pressure of the liquid and $\rho_{sat,l}$ is the density of the liquid at the saturation pressure. ρ_v is the density of the vapor.

The viscosity of the liquid-vapor mixture as proposed by (Beattie and Whalley, 1982) is modeling:

$$\mu = \begin{cases} \mu_l & \rho \geq \rho_{sat,L} \\ \alpha_v\mu_v + (1 - \alpha_v)(1 + 2.5\alpha_v)\mu_l & \rho < \rho_{sat,L} \end{cases} \tag{26}$$

where μ_v and μ_l denote the viscosity of the vapor and liquid, respectively.

1.4 Modified Zwart-Gerber-Belamri cavitation model (Modified-ZGB)

Simulation of flows in hydro turbines and pumps (Asnaghi et al., 2019; Chen et al., 2019; Cheng et al., 2021; Guo et al., 2019) requires modelling of vortex cavitation. In finite mass transfer rate methods, the relevant empirical coefficients can be determined through numerical/experimental results and tuned for different geometries and flow conditions (Anderlini et al., 2020; Liu et al., 2014; Morgut et al., 2011). A simplified factor is extracted from the original rotation-curvature correction (Spalart and Shur, 1997) to identify the vortex region in the nozzle centrally:

$$f^* = \frac{2r^*}{1+r^*},\ r^* = \frac{S}{\Omega} \tag{27}$$

where S is the strain rate tensor and Ω is the vorticity tensor.

According to the previous equations, if the flow has a robust rotational motion, Ω is much larger than S, then the variable f^* approaches to 0. As Ω is about equal to S, f^* is close to 0. When the rotational flow is weak, Ω is much smaller than S, and then f^* is equivalent to 2 approximatively. In the general vortex-induced cavitation, the vorticity tensor plays a vital role in the cavitating flow compared to the shear stress tensor, hence the value of f^* falls in between 0 and 1. Here, a numerical case of string cavitation flow from the previously published paper (Guan et al., 2021b) is employed to reveal the distribution of f^* at different planes in the injector nozzle hole, as shown in Fig .17. Values of f^* increase from inside to outside along the radius of a hole on one certain plane. Moreover, the smaller value of f^* corresponds to the present region of vortex-induced string cavitation, where vorticity dominates relative to the strain rate.

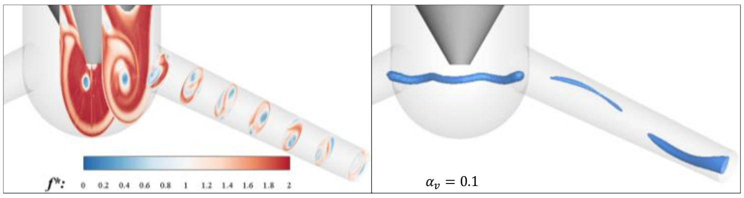

Fig. 17. Distribution of the variable f^*(left) and vapor iso-surface is 0.1 (right) (Guan et al., 2021b).

For the ZGB cavitation model, the modification to the condensation coefficient is employed here. This is because the string cavitation in the sac chamber can develop further downstream, keeping its original trajectory with the decrease of condensation coefficient, which corresponds to the reduction of the mass transport from vapor to liquid (Guo et al., 2018). Similar to the modification form proposed by Asnaghi et al. (Asnaghi et al., 2017), a new modification of cavitation mass transfer source term for vortex-induced cavitation is constructed by authors as follows:

$$\dot{R_c} = cc * F_{\mathrm{cond}} \frac{3\alpha_{\mathrm{v}}\rho_{\mathrm{v}}}{R_{\mathrm{B}}} \sqrt{\frac{2}{3}\frac{(p-p_{\mathrm{v}})}{\rho_{\mathrm{l}}}} \tag{28}$$

$$cc = (1 + t_{\infty} \times \Omega_{ij})^{-1} \tag{29}$$

where cc is applied to adjust and calibrate the mass transfer rate. $t_\infty = L_\infty / U_\infty$ is employed to normalize the vorticity tensor. Ω_{ij} is the antisymmetric tensor of velocity gradient, also known as vorticity tensor.

Appendix 2. Turbulence models

2.1 RANS models and LES model

The RNG $k-\varepsilon$ model devised by Yakhot and Orszag et al. (Yakhot and Orszag, 1986) is similar in form to the standard $k-\varepsilon$ model, while it presents a better prediction in terms of three-dimensional flows with high streamline curvature. The SST $k-\omega$ model is a widely-used model which suggests a hybrid between the $k-\omega$ model in the near-wall region and the $k-\varepsilon$ model in the fully turbulent region (Menter, 1994). The RSM model, also called the second-order or second-moment closure model, is quite complex, while it has the potential to calculate all the mean flow characteristics and Reynolds stresses in the simplest type accurately. Therefore, this model can give accurate predictions for complex flows such as the swirling and stress-induced secondary flows in a more rigorous manner than the widely used two-equation models. Different from the RANS models, the LES model employs a spatial filtering operation determined by the cell size of the computational domain to separate the larger and smaller eddies. Large eddies are resolved directly by the computational mesh, while unresolved small eddies are represented by a sub-grid scale model (SGS).

These models have been introduced and formulated in many researches, which can be addressed to some computational fluid dynamics (CFD) handbooks and published papers for more information (Kopparthy et al., 2020; Koukouvinis et al., 2017; Liu et al., 2020; Pope, 2001; Wilcox, 1998; Xiao and Cinnella, 2019), and will not be repeated here. In contrast, a new hybrid RANS/LES model named the VLES model is discussed below. Different from the LES model, in which the filtering method is the computational mesh size, the filtering operation in the VLES model depends on an adjustable value falling in between the mesh scale and macroscale.

2.2 VLES model

In this VLES model, the formulation is similar to the previous VLES model employed by (Han and Krajnović, 2015; Tiwari et al., 2020), with the difference that the SST $k-\omega$ model is applied here but not $k-\varepsilon$ model and BSL $k-\omega$ model. The governing equations of turbulent kinetic energy and its dissipation rate, which are the same as in the SST $k-\omega$ turbulence model (Menter, 1994), are shown as follows, and the turbulent viscosity is scaled by the resolution control function F_r:

$$\frac{\partial(\rho k)}{\partial t}+\frac{\partial(\rho u_j k)}{\partial x_j}=P_k-\beta^*\rho\omega k+\frac{\partial}{\partial x_j}\left[(\mu+\sigma_k\mu_t)\frac{\partial k}{\partial x_j}\right] \tag{30}$$

$$\frac{\partial(\rho\omega)}{\partial t}+\frac{\partial(\rho u_j\omega)}{\partial x_j}=\frac{\omega}{k}P_k-\beta\rho\omega^2+\frac{\partial}{\partial x_j}\left[(\mu+\sigma_\omega\mu_t)\frac{\partial\omega}{\partial x_j}\right]+2(1-F_1)\frac{\rho\sigma_{\omega 2}}{\omega}\frac{\partial k}{\partial x_j}\frac{\partial\omega}{\partial x_j} \tag{31}$$

$$\mu_t=F_r\frac{\rho k}{\omega}\frac{1}{\mathrm{MAX}[1,\frac{SF_2}{a_1\omega}]} \tag{32}$$

$$F_2=\tanh({\emptyset_2}^2) \tag{33}$$

$$\emptyset_2=\mathrm{MAX}[2\frac{\sqrt{k}}{0.09\omega y},\frac{500\mu}{\rho y^2\omega}] \tag{34}$$

where P_k is the modeled turbulent kinetic energy production, in the form of $P_k=\mu_t S^2$, with S is the modulus of the mean rate-of-strain tensor. a_1 is 0.31 and y is the distance to the nearest wall (Menter, 1994); F_r is the fitting parameter of the VLES model, which represents the ratio of modeled turbulent kinetic energy to the total unresolved turbulent kinetic energy. The formula of F_r can be addressed to the published papers (Han and Krajnović, 2013b, 2015):

$$F_r = MIN[1.0, \left(\frac{1.0 - exp(-\beta_r L_c/L_k)}{1.0 - exp(-\beta_r L_i/L_k)}\right)^2] \tag{35}$$

$$L_c = Cx(\Delta x \Delta y \Delta z)^{1/3},\ L_i = k^{\frac{3}{2}}/(\beta^{**} k\omega),\ L_k = v^{\frac{3}{4}}/(\beta^{**} k\omega)^{1/4} \tag{36}$$

where β_r is 0.002, Cx is 0.61 and β^{**} is 0.09. L_c, L_i, and L_k are the turbulent cut-off length scale, integral length scale, and Kolmogorov length scale, respectively. Δx, Δy and Δz are the mesh scales in the three spatial directions and v is the laminar kinematic viscosity. The parameter F_r has a value between 0 and 1.0 with the variation of mesh resolution, corresponding to the working turbulence models ranging from RANS, LES to DNS on account of different computational mesh resolutions (Han and Krajnović, 2013b, 2015).

References

Abdelsamie, A., Chi, C., Nanjaiah, M., Skenderović, I., Suleiman, S., Thévenin, D., 2021. Direct Numerical Simulation of Turbulent Spray Combustion in the SpraySyn Burner: Impact of Injector Geometry. Flow, Turbulence and Combustion 106, 453-469.

Anderlini, A., Salvetti, M., Agresta, A., Matteucci, L., 2020. Stochastic calibration of cavitation model parameters for simulations of 3-phase injector internal flows. Computers & Fluids 205, 104581.

Andriotis, A., Gavaises, M., Arcoumanis, C., 2008. Vortex flow and cavitation in diesel injector nozzles. Journal of Fluid Mechanics 610, 195-215.

Arcoumanis, C., Flora, H., Gavaises, M., Badami, M., 2000. Cavitation in real-size multi-hole diesel injector nozzles. SAE transactions, 1485-1500.

Arcoumanis, C., Gavaises, M., Argueyrolles, B., Galzin, F., 1999. Modeling of pressure-swirl atomizers for GDI engines. SAE transactions, 516-532.

Arcoumanis, C., Gavaises, M., Nouri, J.M., 1997. Investigation of the flow inside the sac volume and the injection holes of a diesel injector, 13th Annual Conference on Liquid Atomisation and Spray Systems (ILASS-

Europe).

Asnaghi, A., Feymark, A., Bensow, R., 2017. Improvement of cavitation mass transfer modeling based on local flow properties. International Journal of Multiphase Flow 93, 142-157.

Asnaghi, A., Svennberg, U., Bensow, R.E., 2019. Evaluation of curvature correction methods for tip vortex prediction in SST k− ω turbulence model framework. International Journal of Heat and Fluid Flow 75, 135-152.

Battistoni, M., Som, S., Powell, C.F., 2019. Highly resolved Eulerian simulations of fuel spray transients in single and multi-hole injectors: Nozzle flow and near-exit dynamics. Fuel 251, 709-729.

Beattie, D.R., Whalley, P., 1982. Simple two-phase frictional pressure drop calculation method. Int. J. Multiphase Flow;(United Kingdom) 8.

Cao, T., He, Z., El-Seesy, A.I., Guan, W., Wang, Q., 2021. Impact of Enlarged Scales and Continuous Bubbles on Cavitation Patterns of Diesel Nozzles. Atomization and Sprays 31.

Cao, T., He, Z., Si, Z., El-Seesy, A.I., Guan, W., Zhou, H., Wang, Q., 2020a. Optical experimental study on cavitation development with different patterns in diesel injector nozzles at different fuel temperatures. Experiments in Fluids 61, 1-14.

Cao, T., He, Z., Zhang, L., Guan, W., Wang, Q., 2020b. Experimental study on the effect of cavitation on pressure fluctuations in optical diesel nozzles and spray characteristics. Atomization and Sprays 30.

Cao, T., He, Z., Zhou, H., Guan, W., Zhang, L., Wang, Q., 2020c. Experimental study on the effect of vortex cavitation in scaled-up diesel injector nozzles and spray characteristics. Experimental Thermal and Fluid Science 113, 110016.

Celik, I., Cehreli, Z., Yavuz, I., 2005. Index of resolution quality for large eddy simulations.

Chebli, R., Audebert, B., Zhang, G., Coutier-Delgosha, O., 2021. Influence of the turbulence modeling on the simulation of unsteady cavitating flows. Computers & Fluids 221, 104898.

Chen, L., Zhang, L., Peng, X., Shao, X., 2019. Influence of water quality on the tip vortex cavitation inception. Physics of Fluids 31, 023303.

Chen, Z., He, Z., Shang, W., Duan, L., Zhou, H., Guo, G., Guan, W., 2018. Experimental study on the effect of nozzle geometry on string cavitation in real-size optical diesel nozzles and spray characteristics. Fuel 232, 562-571.

Cheng, H., Bai, X., Long, X., Ji, B., Peng, X., Farhat, M., 2020. Large eddy simulation of the tip-leakage cavitating flow with an insight on how cavitation influences vorticity and turbulence. Applied Mathematical Modelling 77, 788-809.

Cheng, H., Long, X., Ji, B., Peng, X., Farhat, M., 2021. A new Euler-Lagrangian cavitation model for tip-vortex cavitation with the effect of non-condensable gas. International Journal of Multiphase Flow 134, 103441.

Chow, J.S., Zilliac, G.G., Bradshaw, P., 1997. Mean and turbulence measurements in the near field of a wingtip vortex. AIAA journal 35, 1561-1567.

Cotel, A.J., Breidenthal, R.E., 1999. Turbulence inside a vortex. Physics of Fluids 11, 3026-3029.

Dittakavi, N., Chunekar, A., Frankel, S., 2010. Large eddy simulation of turbulent-cavitation interactions in a venturi nozzle. Journal of Fluids Engineering 132.

Egerer, C.P., Hickel, S., Schmidt, S.J., Adams, N.A., 2014. Large-eddy simulation of turbulent cavitating flow in a micro channel. Physics of Fluids 26, 085102.

Ehrhard, J., 1999. Untersuchung linearer und nichtlinearer Wirbelviskositätsmodelle zur Berechnung turbulenter Strömungen um Gebäude. VDI-Verlag.

Gavaises, M., 2008. Flow in valve covered orifice nozzles with cylindrical and tapered holes and link to cavitation erosion and engine exhaust emissions. International Journal of Engine Research 9, 435-447.

Gavaises, M., Andriotis, A., 2006. Cavitation inside multi-hole injectors for large diesel engines and its effect on the near-nozzle spray structure. SAE Transactions, 634-647.

Gavaises, M., Andriotis, A., Papoulias, D., Mitroglou, N., Theodorakakos, A., 2009. Characterization of string cavitation in large-scale Diesel nozzles with tapered holes. Physics of fluids 21, 052107.

Gavaises, M., Papoulias, D., Giannadakis, E., Andriotis, A., Mitroglou, N., Theodorakakos, A., 2008. Comparison of cavitation formation and development in Diesel VCO nozzles with cylindrical and converging tapered holes, Conference on Thermo- and Fluid Dynamic Processes in Diesel Engines.

Gavaises, M., Villa, F., Koukouvinis, P., Marengo, M., Franc, J.-P., 2015. Visualisation and les simulation of cavitation cloud formation and collapse in an axisymmetric geometry. International Journal of Multiphase Flow 68, 14-26.

Ghahramani, E., Arabnejad, M.H., Bensow, R.E., 2019. A comparative study between numerical methods in simulation of cavitating bubbles. International Journal of Multiphase Flow 111, 339-359.

Gold, M., Pearson, R., Turner, J., Sykes, D., Stetsyuk, V., De Sercey, G., Crua, C., Murali-Girija, M., Koukouvinis, F., Gavaises, M., 2019. Simulation and measurement of transient fluid phenomena within diesel injection. SAE International Journal of Advances and Current Practices in Mobility 1, 291-305.

Guan, W., He, Z., Duan, L., Cao, T., Sun, S., Zhang, L., 2021a. Optical investigations of nozzle geometrical and dynamic factors on formation and development characteristics of string cavitation with large-scale diesel tapered-hole nozzles. International Journal of Engine Research 22, 3147-3163.

Guan, W., He, Z., Zhang, L., Guo, G., Cao, T., Leng, X., 2021b. Investigations on interactions between vortex flow and the induced string cavitation characteristics in real-size diesel tapered-hole nozzles. Fuel 287, 119535.

Guo, G., He, Z., Chen, Y., Wang, Q., Leng, X., Sun, S., 2017. LES investigations on effects of the residual bubble on the single hole diesel injector jet. International Journal of Heat and Mass Transfer 112, 18-27.

Guo, Q., Huang, X., Qiu, B., 2019. Numerical investigation of the blade tip leakage vortex cavitation in a waterjet pump. Ocean Engineering 187, 106170.

Guo, Q., Zhou, L., Wang, Z., Liu, M., Cheng, H., 2018. Numerical simulation for the tip leakage vortex cavitation. Ocean Engineering 151, 71-81.

Han, X., Krajnović, S., 2013a. An efficient very large eddy simulation model for simulation of turbulent flow. International Journal for Numerical Methods in Fluids 71, 1341-1360.

Han, X., Krajnović, S., 2013b. Very large eddy simulation of passive drag control for a D-shaped cylinder. Journal of fluids engineering 135.

Han, X., Krajnović, S., 2015. Very-large-eddy Simulation based on k-ω model. AIAA Journal 53, 1103-1108.

Hayashi, T., Suzuki, M., Ikemoto, M., 2013. Effects of internal flow in a diesel nozzle on spray combustion. International Journal of Engine Research 14, 646-654.

He, Z., Zhang, Z., Guo, G., Wang, Q., Leng, X., Sun, S., 2016. Visual experiment of transient cavitating flow characteristics in the real-size diesel injector nozzle. International Communications in Heat and Mass Transfer 78, 13-20.

He, Z., Zhong, W., Wang, Q., Jiang, Z., Shao, Z., 2013. Effect of nozzle geometrical and dynamic factors on cavitating and turbulent flow in a diesel multi-hole injector nozzle. International Journal of Thermal Sciences 70, 132-143.

He, Z., Zhou, H., Duan, L., Xu, M., Chen, Z., Cao, T., 2021. Effects of nozzle geometries and needle lift on steadier string cavitation and larger spray angle in common rail diesel injector. International Journal of Engine Research 22, 2673-2688.

Heschl, C., Sanz, W., Klanatsky, P., 2005. Implementation and comparison of different turbulence models for three dimensional wall jets with FLUENT, CFD Forum.

Hu, Y., Kai, R., Kurose, R., Gutheil, E., Olguin, H., 2020. Large eddy simulation of a partially pre-vaporized ethanol reacting spray using the multiphase DTF/flamelet model. International Journal of Multiphase Flow 125, 103216.

Ivings, M., Causon, D., Toro, E., 1998. On Riemann solvers for compressible liquids. International Journal for Numerical Methods in Fluids 28, 395-418.

Jiang, L., Cai, J., Liu, C., 2008. Large-eddy simulation of wing tip vortex in the near field. International Journal of Computational Fluid Dynamics 22, 289-330.

Josserand, C., Rossi, M., 2007. The merging of two co-rotating vortices: a numerical study. European Journal of Mechanics-B/Fluids 26, 779-794.

Karathanassis, I.K., Koukouvinis, P., Lorenzi, M., Kontolatis, E., Li, Z., Wang, J., Mitroglou, N., Gavaises, M., 2017. High-speed x-ray phase-contrast imaging of string cavitation in an enlarged diesel-injector orifice replica, 28th European Conference on Liquid Atomization and Spray Systems.

Karathanassis, I.K., Trickett, K., Koukouvinis, P., Wang, J., Barbour, R., Gavaises, M., 2018. Illustrating the effect of viscoelastic additives on cavitation and turbulence with X-ray imaging. Scientific reports 8, 1-15.

Kim, J.H., Nishida, K., Hiroyasu, H., 1997. Characteristics of the internal flow in a diesel injection nozzle. International Journal of Fluid Mechanics Research 24.

Kinzel, M., Kunz, R., Lindau, J., 2017. An Assessment of CFD Cavitation Models Using Bubble Growth Theory and Bubble Transport Modeling, 17th International Symposium on Transport Phenomena and

Dynamics of Rotating Machinery (ISROMAC2017).

Kolev, N.I., Kolev, N., 2005. Multiphase flow dynamics. Springer.

Kolovos, K., Kyriazis, N., Koukouvinis, P., Vidal, A., Gavaises, M., McDavid, R.M., 2021. Simulation of transient effects in a fuel injector nozzle using real-fluid thermodynamic closure. Applications in Energy and Combustion Science 7, 100037.

Kopparthy, S., Mansour, M., Janiga, G., Thévenin, D., 2020. Numerical investigations of turbulent single-phase and two-phase flows in a diffuser. International Journal of Multiphase Flow 130, 103333.

Koukouvinis, P., Gavaises, M., Li, J., Wang, L., 2016. Large Eddy Simulation of Diesel injector including cavitation effects and correlation to erosion damage. Fuel 175, 26-39.

Koukouvinis, P., Naseri, H., Gavaises, M., 2017. Performance of turbulence and cavitation models in prediction of incipient and developed cavitation. International Journal of Engine Research 18, 333-350.

Koukouvinis, P., Vidal-Roncero, A., Rodriguez, C., Gavaises, M., Pickett, L., 2020. High pressure/high temperature multiphase simulations of dodecane injection to nitrogen: Application on ECN Spray-A. Fuel 275, 117871.

Kumar, A., Ghobadian, A., Nouri, J.M., 2020. Assessment of cavitation models for compressible flows inside a nozzle. Fluids 5, 134.

Kyriazis, N., Koukouvinis, P., Gavaises, M., 2017. Numerical investigation of bubble dynamics using tabulated data. International Journal of Multiphase Flow 93, 158-177.

Lan, Q., Fan, L., Bai, Y., Gu, Y., Wen, L., 2020. Correlation analysis upon the influential factors related to the dynamic response characteristics of pressure amplification piston in the fuel system for a low-speed diesel engine. Fuel 276, 118052.

Laurila, E., Koivisto, S., Kankkunen, A., Saari, K., Maakala, V., Järvinen, M., Vuorinen, V., 2020.

Computational and experimental investigation of a swirl nozzle for viscous fluids. International Journal of Multiphase Flow 128, 103278.

Li, D., He, Z., Xuan, T., Zhong, W., Cao, J., Wang, Q., Wang, P., 2017. Simultaneous capture of liquid length of spray and flame lift-off length for second-generation biodiesel/diesel blended fuel in a constant volume combustion chamber. Fuel 189, 260-269.

Li, X., Li, B., Yu, B., Ren, Y., Chen, B., 2019. Calculation of cavitation evolution and associated turbulent kinetic energy transport around a NACA66 hydrofoil. J Mech Sci Technol 33, 1231-1241.

Liu, H.-l., Wang, J., Wang, Y., Zhang, H., Huang, H., 2014. Influence of the empirical coefficients of cavitation model on predicting cavitating flow in the centrifugal pump. International Journal of Naval Architecture and Ocean Engineering 6, 119-131.

Liu, Z.-h., Wang, B.-l., Peng, X.-x., Liu, D.-c., 2016. Calculation of tip vortex cavitation flows around three-dimensional hydrofoils and propellers using a nonlinear k-ε turbulence model. Journal of Hydrodynamics, Ser. B 28, 227-237.

Liu, Z., Wijeyakulasuriya, S., Mashayekh, A., Chai, X., 2020. Investigation of Reynolds Stress Model for Complex Flow Using CONVERGE. SAE Technical Paper.

Menter, F.R., 1994. Two-equation eddy-viscosity turbulence models for engineering applications. AIAA journal 32, 1598-1605.

Mithun, M.-G., Koukouvinis, P., Gavaises, M., 2018. Numerical simulation of cavitation and atomization using a fully compressible three-phase model. Physical Review Fluids 3, 064304.

Moon, S., Huang, W., Wang, J., 2019. First observation and characterization of vortex flow in steel micronozzles for high-pressure diesel injection. Experimental Thermal and Fluid Science 105, 342-348.

Morgut, M., Nobile, E., Biluš, I., 2011. Comparison of mass transfer models for the numerical prediction of sheet cavitation around a hydrofoil. International Journal of Multiphase Flow 37, 620-626.

Naseri, H., Koukouvinis, P., Malgarinos, I., Gavaises, M., 2018. On viscoelastic cavitating flows: A numerical study. Physics of Fluids 30, 033102.

Ohta, T., Sugiura, R., 2019. Numerical prediction of interaction between turbulence structures and vortex cavitation. Journal of Turbulence 20, 599-625.

Papoutsakis, A., Koukouvinis, P., Gavaises, M., 2020. Solution of cavitating compressible flows using Discontinuous Galerkin discretisation. Journal of Computational Physics 410, 109377.

Parkin, B.R., 1952. Scale effects in cavitating flow, California Institute of Technology. California Institute of Technology.

Payri, R., Salvador, F., Gimeno, J., Bracho, G., 2011. The effect of temperature and pressure on thermodynamic properties of diesel and biodiesel fuels. Fuel 90, 1172-1180.

Piscaglia, F., Giussani, F., Hèlie, J., Lamarque, N., Aithal, S.M., 2021. Vortex Flow and Cavitation in Liquid Injection: A Comparison between High-Fidelity CFD Simulations and Experimental Visualizations on Transparent Nozzle Replicas. International Journal of Multiphase Flow 138, 103605.

Pope, S.B., 2001. Turbulent flows. IOP Publishing.

Pope, S.B., 2004. Ten questions concerning the large-eddy simulation of turbulent flows. New journal of Physics 6, 35.

Prasetya, R., Sou, A., Oki, J., Nakashima, A., Nishida, K., Wada, Y., Ueki, Y., Yokohata, H., 2021. Three-dimensional flow structure and string cavitation in a fuel injector and their effects on discharged liquid jet. International Journal of Engine Research 22, 243-256.

Pratama, R.H., Sou, A., Katsui, T., Nishio, S., 2017. String cavitation in a fuel injector. Atomization and Sprays 27.

Reboud, J.-L., Stutz, B., Coutier, O., 1998. Two phase flow structure of cavitation: experiment and modeling of unsteady effects, 3rd International Symposium on Cavitation CAV1998, Grenoble, France.

Rinaldo, L., Miorini, Huixuan, Wu, Joseph, Katz, 2012. The Internal Structure of the Tip Leakage Vortex Within the Rotor of an Axial Waterjet Pump, Asme Turbo Expo: Power for Land, Sea, & Air, pp. 031018.031011-031018.031012.

Rojanaratanangkule, W., Tunkaew, J., 2016. Direct Numerical Simulation of a Counter-Rotating Vortex Pair Embedded in Turbulence, 20th Australasian Fluid Mechanics Conference, Perth, Australia.

Roth, H., Gavaises, M., Arcoumanis, C., 2002. Cavitation initiation, its development and link with flow turbulence in diesel injector nozzles. SAE Transactions, 561-580.

Salemi, R., Koukouvinis, P., Strotos, G., McDavid, R., Wang, L., Li, J., Marengo, M., Gavaises, M., 2015. Evaluation of friction heating in cavitating high pressure Diesel injector nozzles, Journal of Physics: Conference Series. IOP Publishing, p. 012083.

Santos, E.G., Shi, J., Gavaises, M., Soteriou, C., Winterbourn, M., Bauer, W., 2020. Investigation of cavitation and air entrainment during pilot injection in real-size multi-hole diesel nozzles. Fuel 263, 116746.

Sauer, J., Schnerr, G.H., 2000. Unsteady cavitating flow-a new cavitation model based on a modified front capturing method and bubble dynamics, Proceedings of 2000 ASME fluid engineering summer conference, pp. 1073-1079.

Shi, J., Aguado, P., Dober, G., Guerrassi, N., Bauer, W., Lai, M., 2016. Using LES and x-ray imaging to understand the influence of injection hole geometry on Diesel spray formation, THIESEL 2016 Conf Thermo-Fluid Dyn Process Diesel EnginesConference Thermo Fluid Dyn, pp. 1-21.

Shur, M.L., Strelets, M.K., Travin, A.K., Spalart, P.R., 2000. Turbulence modeling in rotating and curved channels: assessing the Spalart-Shur correction. AIAA journal 38, 784-792.

Som, S., Ramirez, A.I., Longman, D.E., Aggarwal, S.K., 2011. Effect of nozzle orifice geometry on spray, combustion, and emission characteristics under diesel engine conditions. Fuel 90, 1267-1276.

Sou, A., Biçer, B., Tomiyama, A., 2014. Numerical simulation of incipient cavitation flow in a nozzle of fuel injector. Computers & Fluids 103, 42-48.

Spalart, P., Shur, M., 1997. On the sensitization of turbulence models to rotation and curvature. Aerospace Science and Technology 1, 297-302.

Strotos, G., Koukouvinis, P., Theodorakakos, A., Gavaises, M., Bergeles, G., 2015. Transient heating effects in high pressure Diesel injector nozzles. International Journal of Heat and Fluid Flow 51, 257-267.

Tiwari, P., Xia, Z., Han, X., 2020. Comparison of VLES and LES Turbulence Modeling for Swirling Turbulent Flow. Journal of Applied Fluid Mechanics 13, 1107-1116.

Trummler, T., Schmidt, S.J., Adams, N.A., 2020. Investigation of condensation shocks and re-entrant jet dynamics in a cavitating nozzle flow by Large-Eddy Simulation. International Journal of Multiphase Flow 125, 103215.

Trummler, T., Schmidt, S.J., Adams, N.A., 2021. Effect of stand-off distance and spatial resolution on the pressure impact of near-wall vapor bubble collapses. International Journal of Multiphase Flow 141, 103618.

Wang, B., Liu, Z., 2018. Numerical Simulations of Tip Leakage Vortex Cavitation Flows Around a NACA0009 Hydrofoil.

Wang, J., He, Z., Duan, L., Zhou, H., Zhong, W., Guo, G., 2021. Effect of diesel/gasoline/HCB blends and temperature on string cavitating flow in common-rail injector nozzle. Fuel 304, 121402.

Wang, P., Jia, M., Zhang, Y., Xu, G., Chang, Y., Xu, Z., 2019. Development of a decoupling physical-chemical surrogate (DPCS) model for simulation of the spray and combustion of multi-component biodiesel fuels. Fuel 240, 16-30.

Watanabe, H., Nishikori, M., Hayashi, T., Suzuki, M., Kakehashi, N., Ikemoto, M., 2015. Visualization analysis of relationship between vortex flow and cavitation behavior in diesel nozzle. International Journal of Engine Research 16, 5-12.

Wilcox, D.C., 1998. Turbulence modeling for CFD. DCW industries La Canada, CA.

Xiao, H., Cinnella, P., 2019. Quantification of model uncertainty in RANS simulations: A review. Progress in Aerospace Sciences 108, 1-31.

Yakhot, V., Orszag, S.A., 1986. Renormalization group analysis of turbulence. I. Basic theory. Journal of scientific computing 1, 3-51.

Yamamoto, Y., Watanabe, S., Tsuda, S., 2015. A simple cavitation model for unsteady simulation and its application to cavitating flow in two-dimensional convergent-divergent nozzle, IOP Conference Series: Materials Science and Engineering. IOP Publishing, p. 022009.

Zhang, B., Popinet, S., Ling, Y., 2020. Modeling and detailed numerical simulation of the primary breakup of a gasoline surrogate jet under non-evaporative operating conditions. International Journal of Multiphase Flow 130, 103362.

Zhang, L., Wang, Q., Guan, W., Cao, T., Duan, L., Pachiannan, T., He, Z., 2019. Large eddy simulations on asymmetrical atomization of the elliptical jet with cavitation. Atomization and Sprays 29.

Zhang, X., He, Z., Wang, Q., Tao, X., Zhou, Z., Xia, X., Zhang, W., 2018. Effect of fuel temperature on cavitation flow inside vertical multi-hole nozzles and spray characteristics with different nozzle geometries. Experimental Thermal and Fluid Science 91, 374-387.

Zhao, Y., Wang, G., Huang, B., 2016. A cavitation model for computations of unsteady cavitating flows. Acta Mechanica Sinica 32, 273-283.

Zwart, P.J., Gerber, A.G., Belamri, T., 2004. A two-phase flow model for predicting cavitation dynamics, Fifth international conference on multiphase flow, Yokohama, Japan.